Astronomy & Astrophysics manuscript no. udry2017
May 16, 2017

The HARPS search for southern extra-solar planets.

XXXVI. Eight HARPS multi-planet systems hosting 20 super-Earth and Neptune-mass companions ⋆ ⋆⋆ ⋆⋆⋆

S. Udry[1], X. Dumusque[1], C. Lovis[1], D. Ségransan[1], R. Diaz[1], W. Benz[2], F. Bouchy[1,3], A. Coffinet[1], G. Lo Curto[4], M. Mayor[1], C. Mordasini[2], F. Motalebi[1], F. Pepe[1], D. Queloz[1], N.C. Santos[5,6], A. Wyttenbach[1], R. Alonso[7], A. Collier Cameron[8], M. Deleuil[3], P. Figueira[5], M. Gillon[9], C. Moutou[3,10], D. Pollacco[11], and E. Pompei[4]

[1] Observatoire astronomique de l'Université de Genève, 51 ch. des Maillettes, CH-1290 Versoix, Switzerland
[2] Physikalisches Institut, Universitat Bern, Silderstrasse 5, CH-3012 Bern, Switzerland
[3] Aix Marseille Université, CNRS, LAM (Laboratoire d'Astrophysique de Marseille) UMR 7326, 13388, Marseille, France
[4] European Southern Observatory, Karl-Schwarzschild-Str. 2, D-85748 Garching bei München, Germany
[5] Instituto de Astrofísica e Ciências do Espaço, Universidade do Porto, CAUP, Rua das Estrelas, 4150-762 Porto, Portugal
[6] Departamento de Física e Astronomia, Faculdade de Ciências, Universidade do Porto, Rua do Campo Alegre, 4169-007 Porto, Portugal
[7] Instituto de Astrofisica de Canarias, 38025, La Laguna, Tenerife, Spain
[8] School of Physics and Astronomy, University of St Andrews, North Haugh, St Andrews, Fife KY16 9SS
[9] Institut d'Astrophysique et de Géophysique, Université de Liège, Allée du 6 Août 17, Bat. B5C, 4000, Liège, Belgium
[10] Canada France Hawaii Telescope Corporation, Kamuela, 96743, USA
[11] Department of Physics, University of Warwick, Coventry, CV4 7AL, UK

Received XXX; accepted XXX

ABSTRACT

Context. We present radial-velocity measurement of eight stars observed with the HARPS Echelle spectrograph mounted on the 3.6-m telescope in La Silla (ESO, Chile). Data span more than ten years and highlight the long-term stability of the instrument.
Aims. We search for potential planets orbiting HD 20003, HD 20781, HD 21693, HD 31527, HD 45184, HD 51608, HD 134060 and HD 136352 to increase the number of known planetary systems and thus better constrain exoplanet statistics.
Methods. After a preliminary phase looking for signals using generalized Lomb-Scargle periodograms, we perform a careful analysis of all signals to separate *bona-fide* planets from spurious signals induced by stellar activity and instrumental systematics. We finally secure the detection of all planets using the efficient MCMC available on the Data and Analysis Center for Exoplanets (DACE web-platform), using model comparison whenever necessary.
Results. In total, we report the detection of twenty new super-Earth to Neptune-mass planets, with minimum masses ranging from 2 to 30 M_{Earth}, and periods ranging from 3 to 1300 days. By including CORALIE and HARPS measurements of HD20782 to the already published data, we also improve the characterization of the extremely eccentric Jupiter orbiting this host.

Key words. Planetary systems – Techniques: RVs – Techniques: spectroscopy – Methods: data analysis – Stars: individual: HD 20003, HD 20781, HD 20782, HD 21693, HD 31527, HD 45184, HD 51608, HD 134060, HD 136352

1. Introduction

The radial velocity (RV) planet search programs with the HARPS spectrograph on the ESO 3.6-m telescope (Pepe et al. 2000; Mayor et al. 2003) have contributed in a tremendous way to our knowledge of the population of small-mass planets around solar-type stars. The HARPS planet-search program on Guaranteed Time Observations (GTO, PI: M. Mayor) was on-going for 6 years between autumn 2003 and spring 2009. The high-precision part of this HARPS GTO survey aimed at the detection of very low-mass planets in a sample of quiet solar-type stars already screened for giant planets at a lower precision with the CORALIE Echelle spectrograph mounted on the 1.2-m Swiss telescope on the same site (Udry et al. 2000). The GTO was then continued within the ESO Large Programs 183.C-0972, 183.C-1005 and 192.C-0852 (PI: S. Udry), from 2009 and 2016.

Within these programs, HARPS has allowed for the detection (or has contributed to the detection) of more than 100 extra-solar planet candidates (see detections in Díaz et al. 2016; Moutou et al. 2015; Lo Curto et al. 2013; Dumusque et al. 2011a; Mayor et al. 2011; Pepe et al. 2011; Moutou et al. 2011; Lovis et al. 2011b). In particular, HARPS has unveiled the existence of a large population of low-mass planets including super-Earths and

Send offprint requests to: Stéphane Udry, e-mail: Stephane.Udry@unige.ch

⋆ Based on observations made with the HARPS instrument on the ESO 3.6 m telescope at La Silla Observatory under the GTO program 072.C-0488 and Large program 193.C-0972/193.C-1005/.

⋆⋆ The analysis of the radial-velocity measurements were performed using the Data and Analysis Center for Exoplanets (DACE) web interface available for the community at the following address: https://dace.unige.ch/

⋆⋆⋆ The HARPS RV measurements discussed in this paper are available in electronic form at the CDS via anonymous ftp to cdsarc.u-strasbg.fr (130.79.128.5) or via http://cdsweb.u-strasbg.fr/cgi-bin/qcat?J/A+A/.

hot Neptunes previous to the launch of the *Kepler* satellite which provided us with an overwhelming sample of thousands of small-size transiting candidates (Coughlin et al. 2015; Mullally et al. 2015; Borucki et al. 2011; Batalha et al. 2011). A preliminary analysis of the HARPS data showed at that time that at least 30 % of solar-type stars were hosting low-mass planets on short-period orbits (Lovis et al. 2009, less than 50 days). A comprehensive analysis of our high-precision sample combined with 18 years of data from CORALIE allowed us later to precise this occurrence rate: about 50% of the stars surveyed have planets with masses below 50 Earth masses on short to moderate period orbits (Mayor et al. 2011). Furthermore, a large fraction of those planets are in multi-planetary systems. This preliminary statistics of hot super-Earth and Neptune frequency is now beautifully confirmed by the impressive results of the *Kepler* mission.

With the RV technique, the variation of the velocity of the central star due to the perturbing effect of small-mass planets becomes very small, of the order or even smaller than the uncertainties of the measurements. The problems to solve and characterise the individual systems are then multi-fold, requiring to disentangle the planetary from the stellar, instrumental, and statistical noise effects. Efficient statistical techniques, mainly based on a Bayesian approach, have been developed to optimise the process and thus the outcome of ongoing RV surveys (see Dumusque et al. 2016, and references therein). A large number of observations is however paramount for a complete probe of the planetary content of the system, and to take full advantage of the developed technique of analysis. In this context, focusing on the most observed, closest and brightest stars, an on-going HARPS LP (198.C-0836) is continuing the original observing efforts and providing us with an unprecedented sample of well observed stars. In this paper we describe 8 planetary systems hosting 20 planets. The detection of these planets had been announced in Mayor et al. (2011) studying statistical properties of the systems discovered with HARPS. Most of them are super-Earths and Neptunian planets on relatively short periods, and member of a multi-planet system. We present here one 4-planet system around HD 20781, two 3-planet systems around HD 31527 and HD 136352, and five 2-planet systems around HD 20003, HD 21693, HD 45184, HD 51608, and HD 134060. In addition, we give updated orbital parameters for the very eccentric planet orbiting HD 20782 (Jones et al. 2006), derived by combining HARPS, CORALIE and the published UCLES data. The paper is organised as follows. In Sec. 2 we discuss the primary star properties. RV measurements and orbital solutions of each system are presented in Sects. 3 and 5, while Sec. 4 describes the framework used for analysing the data. We provide concluding remarks in Sec. 6.

2. Stellar characteristics

This section provides basic information about the stars hosting the planets presented in this paper. Effective temperatures, gravity and metallicities are derived from the spectroscopic analysis of HARPS spectra from Sousa et al. (2008). We used the improved Hipparcos astrometric parallaxes re-derived by van Leeuwen (2007) to determine the absolute V-band magnitude using the apparent visual magnitude from Hipparcos (ESA 1997). Metallicities, together with the effective temperatures and M_V are then used to estimate basic stellar parameters (ages, masses) using theoretical isochrones from the grid of Geneva stellar evolution models, including a Bayesian estimation method (Mowlavi et al. 2012).

Individual spectra were also used to derive the Bisector Inverse Slope (BIS) of the HARPS Cross-Correlation Function (CCF, Pepe et al. 2002; Baranne et al. 1996), as defined by Queloz et al. (2000), the Full Width at Half Maximum (FWHM) and the Contrast of the CCF, as well as a measurement of the chromospheric activity S-index, $\log(R'_{HK})$ and Hα, following a similar approach as used by Santos et al. (2000) and Gomes da Silva et al. (2011). Using Mamajek & Hillenbrand (2008), we estimate rotational periods for our stars, from the empirical correlation of stellar rotation and chromospheric activity index (Noyes et al. 1984). We also derived the $v \sin(i)$ from a calibration of the FWHM of the HARPS CCF following a standard approach (e.g. Santos et al. 2002). All those extra indicators are used to disentangle small-amplitude planetary signals from stellar noise (see e.g. the case of the active star CoRoT-7 and α Centauri B, Queloz et al. 2009; Dumusque et al. 2012).

By construction of the HARPS high-precision sample from low-activity stars in the CORALIE volume-limited planet-search sample, the eight stars discussed here present low activity levels. The average values of the $\log(R'_{HK})$ activity index, estimated from the chromospheric re-emission in the Ca II H and K lines at λ = 3933.66 Å and 3968.47 Å, are low, ranging from −5.01 to −4.87. Activity-induced RV jitter on stellar rotation time scales, due to spots and faculae on the stellar surface, is thus expected to remain at a low level. The potential influence of stellar activity on RVs is nevertheless scrutinised closely when long-term variation of activity indexes are observed (magnetic cycle) or when the planetary and stellar rotation periods are of similar values.

3. HARPS RV measurements

RVs presented here have been obtained with the HARPS high-resolution spectrograph installed on the 3.6m ESO telescope at La Silla Observatory (Mayor et al. 2003). The long-term $\mathrm{m\,s^{-1}}$RV precision is ensured by nightly ThAr calibrations (Lovis et al. 2008). On the short timescale of a night, the high precision is obtained using simultaneous ThAr reference (from 2003 to 2013) or Fabry-Perot étalon reference (since 2013) calibrations.

Low-mass planets are very often found in multi-planet systems (e.g. Lovis et al. 2006, 2011b; Udry & Santos 2007; Mayor et al. 2009; Vogt et al. 2010; Díaz et al. 2015; Motalebi et al. 2015; Latham et al. 2011; Lissauer et al. 2011, 2014; Fabrycky et al. 2014, for RV results and *Kepler* findings). The several components in the system give rise to often complex, low-amplitude RV signals, not easy to solve for. The optimal observing strategy for a given star is a priori unknown, the relevant planetary periods possibly extending over three orders of magnitude. An adequate and efficient observing strategy has been developed coping with the need to accumulate a large number of measurements and to probe different timescales of variation. We typically follow our targets every night during a few initial observing runs, and after gathering a few dozen observations we compare the observed jitter with the expected one depending on the stellar spectral type. If more jitter is observed, we continue monitoring at the same cadence when high-frequency variations are seen, or we adapt the frequency to possible variations at longer timescales.

The majority of the stars in our HARPS high-precision program have been followed since 2003, gathering observations spanning more than 11 years. We are not considering here observations obtained after May 2015 when a major upgrade of the instrument was implemented (change of the optical fibres), which produced an offset in the RVs but also in the activity indicators derived. To prove the long-term stability of the instrument,

Table 1. Observed and inferred stellar parameters for the stars hosting planetary systems described in this paper.

Parameters	HD 20003	HD 20781[a]	HD 21693	HD 31527	HD 45184	HD 51608	HD 134060	HD 136352
Sp. Type[(1)]	G8V	K0V	G8V	G2V	G1.5V	G7V	G3IV	G4V
V[(1)]	8.39	8.48	7.95	7.49	6.37	8.17	6.29	5.65
$B-V$[(1)]	0.77	0.82	0.76	0.61	0.62	0.77	0.62	0.63
π [mas][(1)]	22.83±0.65	28.27±1.08	30.88±0.49	25.93±0.60	45.70±0.40	28.71±0.51	41.32±0.45	67.51±0.39
M_V[(1)]	5.22	5.70	5.40	4.87	4.65	5.51	4.38	4.83
$T_{\rm eff}$ [K][(2)]	5494±27	5256±29	5430±26	5898 ±13	5869±14	5358±22	5966±14	5664±14
$[Fe/H]$[(2)]	0.04 ± 0.02	−0.11 ± 0.02	0.0 ± 0.02	−0.17 ± 0.01	0.04 ± 0.01	−0.07 ± 0.01	0.14 ± 0.01	−0.34 ± 0.01
$\log(g)$[(2)]	4.41±0.05	4.37±0.05	4.37 ±0.04	4.45±0.02	4.47±0.02	4.36±0.05	4.43 ±0.03	4.39±0.02
$M_\star$ [$M_\odot$][(2)]	0.875	0.70	0.80	0.96	1.03	0.80	1.095	0.81
$L_\star$ [$L_\odot$][(2)]	0.72±0.03	0.49±0.04	0.62±0.02	1.20±0.03	1.13±0.01	0.57±0.02	1.44±0.02	0.99±0.01
$\log(R'_{HK})$[(3)]	−4.97±0.05	−5.03±0.01	−4.91±0.05	−4.96±0.01	−4.91±0.01	−4.98±0.02	−5.00±0.01	−4.95±0.01
$v \sin(i)$ [km s^{-1}][(3)]	1.9	1.1	1.6	1.9	2.1	1.3	2.6	< 1
P_{rot} [days][(4)]	38.9±4.0	46.8±4.4	35.2±4.0	20.3±2.9	21.5±3.0	40.0±4.0	23.0±2.9	23.8±3.1

Notes. (1) Astrometric and visual photometric data from the Hipparcos Catalogs (ESA 1997; van Leeuwen 2007). (2) From Sousa et al. (2008) spectroscopic analysis. (3) Parameter derived using HARPS spectra or CCF. (4) From the calibration of Mamajek & Hillenbrand (2008).
[a] HD 20782, the stellar visual companion of HD 20781, hosts a planet as well. The corresponding stellar parameters are given in Jones et al. (2006).

Table 2. HARPS RVs and parameters inferred from the spectra and cross correlation functions for the 9 planet-host stars discussed in the paper.

	JDB [-2400000 days]	RV [km/s]	ε_{RV} [m/s]	FWHM [km/s]	Contrast [%]	BIS [m/s]	$\log(R'_{HK})$	SN50
HD 20003	52984.634366	-16.10292	0.00166	6.86779	52.64	-0.03315	-4.97	59.9
HD 20003	53294.749990	-16.10914	0.00118	6.88617	52.71	-0.03659	-4.95	66.6
HD 20003	53668.758620	-16.09580	0.00089	6.89694	52.39	-0.03234	-4.86	88.9
...								

we decided here to perform this cutoff. We also removed measurements done on night JD=2455115 and 2455399 as an unexplained instrumental systematic produced RV measurements that were off by more than 10 sigma on several stars observed those nights. Each RV measurement corresponds normally to a 15-minute HARPS exposure. This long exposure time allows to mitigate the short-timescale variations induced by stellar oscillations and therefore to improve RV precision (Dumusque et al. 2011d). For bright stars ($V \leq 6.5$), several exposures are made within 15 minutes to keep the same stellar oscillation mitigating strategy without reaching the saturation level of the detector. The different time series presented in this paper are composed of binned points calculated through a weighted average of all points taken within an hour, so that all the observations taken within 15 minutes are binned together. The stars presented here have between 178 and 245 observations typically spread over ∼4000 days and with a sampling allowing the detection of planets with periods from below 1 day to the full span of the measurements. The obtained SNR at 550 nm typically ranges from 100 to 250 (up to 400 for HD 134060), depending on the star and weather conditions. The corresponding quantified uncertainties on the RVs range then from 0.33 to 0.76 m s^{-1}, including photon noise, calibration errors and instrumental drift uncertainty (see Table 3). This does not include other instrumental systematics like telescope centering and guiding errors, which are expected to be small but difficult to estimate. Possible additional errors not included in this estimate might originate from the RV intrinsic variability of the star (jitter) due to stellar oscillations, granulation (Dravins 1982; Dumusque et al. 2011d) and magnetic activity (Dumusque et al. 2014b, 2011c,b; Lovis et al. 2011a; Meunier et al. 2010; Desort et al. 2007; Saar & Donahue 1997). Those extra errors induced by instrumental systematics or stellar signals will be taken into account when modeling the RVs (see Sec. 4).

The final one-hour binned HARPS RV and $\log(R'_{HK})$ measurements are displayed in the left column of Fig. 1 for the 8 planet-host stars discussed in the paper. These velocities and the parameters inferred from the spectra and cross correlation functions are provided in electronic form at CDS. A sample of these data is provided in Table 2. The statistics of the RV series are listed in Table 3.

4. General approach of the data analysis

The data analysis presented in this paper is performed using a set of online tools available from the DACE platform[1]. The RV tool on this platform allows to upload any RV measurements and then perform a multiple Keplerian adjustment to the data using the approach described in Delisle et al. (2016). Once preliminary Keplerian plus drift parameters are found using this iterative ap-

[1] The DACE platform is available at http://dace.unige.ch while the online tools to analyse radial-velocity data can be found in the section Observations=>RVs

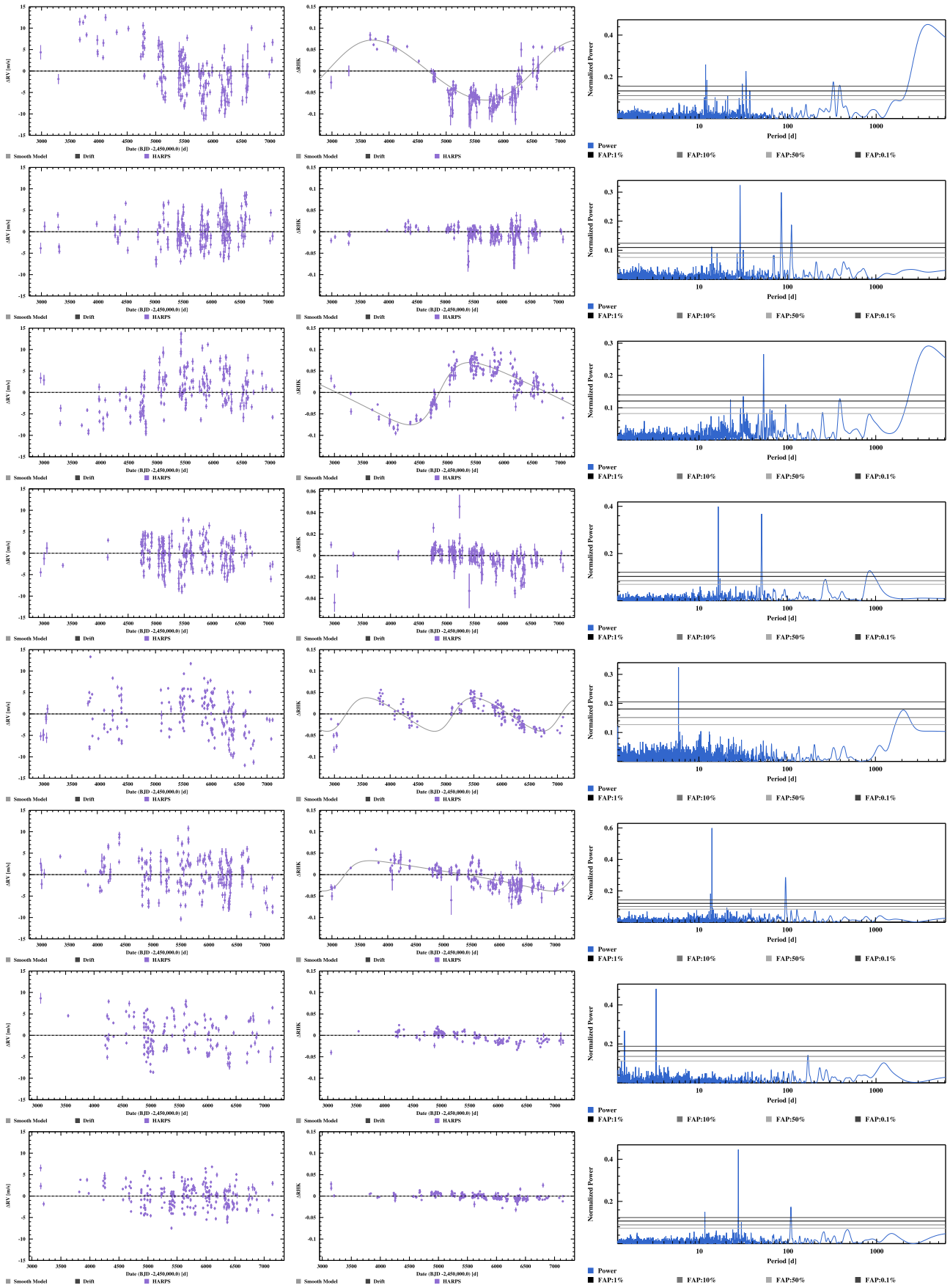

Fig. 1. Left column: From top to bottom, HARPS RV measurements as a function of barycentric Julian Date obtained for HD 20003, HD 20781, HD 21693, HD 31527, HD 45184, HD 51608, HD 134060 and HD 136352. Middle column: log(R'_{HK})activity indicator as a function of time. Right column: GLS periodogram of the corresponding RV measurements.

Table 3. General statistics of the HARPS observations of the planet-host stars presented in this paper, with the number of individual spectrum observed, <S/N> the average signal-to-noise ratio at 550 nm of those spectra, the number of measurement obtained after binning the data over 1 hour, ΔT the time span of the observations, σ_{RV} the rms value of the RV set and $< \varepsilon_{RV} >$ the mean RV photon-noise error.

	N_{spectr}	< SNR > 550 nm	N_{meas} 1-hour bin	ΔT [days]	σ_{RV} [m/s]	$< \varepsilon_{RV} >$ [m/s]
HD 20003	184	110	184	4063	5.35	0.74
HD 20781	225	112	216	4093	3.41	0.76
HD 20782[a]	71	181	68	4111	36.86	0.56
HD 21693	210	141	210	4106	4.72	0.60
HD 31527	256	180	245	4135	3.19	0.64
HD 45184	308	221	178	4160	4.72	0.41
HD 51608	218	133	216	4158	4.07	0.62
HD 134060	335	199	155	4083	3.68	0.40
HD 136352	649	231	240	3993	2.74	0.33

Notes. [a] Star already known as a planet host for which we give here an updated orbit including HARPS observations.

proach, it is possible to run a full Bayesian MCMC analysis using an efficient algorithm (Díaz et al. 2016, 2014).

For each system, we performed a full MCMC analysis, probing the following set of variables for planetary signals: $\log P$, $\log K$, $\sqrt{e}\cos\omega$, $\sqrt{e}\sin\omega$ and λ_0, each one corresponding to the period, the RV semi-amplitude, the eccentricity, the argument of periastron and the mean longitude at a given reference epoch. We used $\sqrt{e}\cos\omega$ and $\sqrt{e}\sin\omega$ as free parameters rather than the eccentricity and the argument of periastron because they translate into a uniform prior in eccentricity (Anderson et al. 2011). The mean longitude (λ_0) is also preferred as a free parameter (instead of the mean anomaly or the date of passage through periastron) since this quantity is not degenerated at low eccentricities.

When no magnetic activity can be seen in the different activity observables (S-index, $\log(R'_{HK})$, Hα-index), we fitted a RV model composed of Keplerians plus a polynomial up to the second order. The MCMC analysis is performed with uniform priors for all variables, with the exception of the stellar mass for which a Gaussian prior is used based on the information given in Table 1. We chose an error in stellar mass of 0.1 $M_\odot$ for all systems to propagate the stellar mass error to the estimation of the planet masses. To take into account uncertainty due to instrumental systematics and/or stellar signals not estimated by the reduction pipeline, we included in the MCMC analysis a white-noise jitter parameter, σ_{JIT}, that is quadratically added to the individual RV error bars.

When a magnetic cycle is detected in the different activity observables (S-index, $\log(R'_{HK})$, Hα-index), we decided, in addition to the model described above, to include two extra components in our RV model to account for the RV variation induced by this magnetic cycle. As explained in Meunier et al. (2016), Lovis et al. (2011a) and Dumusque et al. (2011a), the variation of the total filling factor of spots and faculae along a magnetic cycle change the total amount of stellar convective blueshift, as it is reduced inside spots and faculae due to strong magnetic fields, which thus change the absolute RV of the star. A positive correlation between the different activity observables and the RV is thus expected. In this paper, we decided to use the method proposed by Meunier & Lagrange (2013) to mitigate the impact of magnetic cycles, i.e. to adjust a linear correlation between RV and one of the activity index. Here we decided to use the $\log(R'_{HK})$ (Vaughan et al. 1978; Wilson 1968; Noyes et al. 1984). More spots and faculae are present on the stellar surface during high-activity phases of the magnetic cycle, which implies a stronger stellar jitter due to those surface features coming in and out of view. To account for this stellar jitter that changes in amplitude along the magnetic cycle, we included in the MCMC analysis two extra white-noise jitter parameters, $\sigma_{JIT\,LOW}$ and $\sigma_{JIT\,HIGH}$, that correspond to the jitter during the minimum and the maximum phases of the magnetic cycle. We therefore replace σ_{JIT} described in the precedent paragraph by $\sigma_{JIT\,LOW} + (\sigma_{JIT\,HIGH} - \sigma_{JIT\,LOW})$.norm($\log(R'_{HK})$), where norm($\log(R'_{HK})$) corresponds to $\log(R'_{HK})$ normalized from 0 to 1. For each RV measurement, a new jitter parameter is derived according to the activity level and is quadratically added to the corresponding RV error bar. This is similar to the approach adopted in Díaz et al. (2016). The list of all the parameters probed by our MCMC is given in Table 4.

Before running a full MCMC analysis to obtain reliable posteriors for the orbital parameters of the planets present in the RV measurements, we first iteratively look for significant signals in the data using the approach of Delisle et al. (2016), which gives us a good approximation of the orbital parameters that are used as initial conditions for the MCMC analysis. The iterative approach follow several independent but complementary steps.

4.1. Removing long-term trends

Long-term trends in the data, due either to long-period companions (stellar or planetary) or magnetic cycles (Dumusque et al. 2011b; Lovis et al. 2011a), perturb the detection of planets on shorter periods, due to significant signals at long-period in the Generalized Lomb-Scargle periodogram (GLS, Zechmeister & Kürster 2009; Scargle 1982), and aliases of such signals that appear at shorter periods. We fit a polynomial up to the second order to account for a non-resolved long-period companion. In addition, if a significant long-period signal is seen in the GLS periodogram of the calcium activity $\log(R'_{HK})$, we fit the RVs with a polynomial up to the second order, plus we add to the model the best Keplerian fit to the $\log(R'_{HK})$ leaving only the amplitude as a free parameter. Note that when correcting magnetic cycle effect in RVs when adopting a step-by-step approach, we do not consider a simple linear correlation between RV and $\log(R'_{HK})$ as explained above because significant planetary signals not yet removed from the data might destroy any existing correlation. There is no a priori reason why the magnetic cycle should look like a Keplerian, however a Keplerien has more degrees of freedom than a simple sinusoid and can therefore better estimate the long-term variation seen in $\log(R'_{HK})$. Regarding signal significance, a signal is considered worth looking into when its p-value, which gives the probability that the signal appears just by chance, is smaller or equal to a chosen threshold. Experience has shown us that a signal with a p-value smaller than 1 % is worth looking into details. Note that in this paper, p-values are estimated in a Monte Carlo approach by bootstrapping 10000 times the dates of the observations.

4.2. Detection of periodic signals in the data

– Planetary signals are searched for in the GLS periodogram of the RV residuals after correcting long-term trends. As for magnetic cycles, we consider a signal as significant if its p-value is smaller than 1%[2]. If the p-values of some signals in the GLS periodogram are smaller than 1%, we adjust a Ke-

[2] The goal of our program is to derive reliable statistical distributions of orbital and planet properties that can be used to constrain planet for-

Table 4. List of parameters probed by the MCMC. The symbols $\mathcal{U}$ and $\mathcal{N}$ used for the priors definition stands for uniform and normal distributions, respectively.

Parameters	Units	Priors	Description	Range
Parameters probed by MCMC without magnetic cycle				
$M_\star$	[$M_\odot$]	$\mathcal{N}(M_\star,0.1)$	stellar mass ($M_\star$ can be found in Table 1)	
σ_X	[m s^{-1}]	$\mathcal{U}$	instrumental jitter of instrument X	]-∞,∞[
σ_{JIT}	[m s^{-1}]	$\mathcal{U}$	stellar jitter (If only one instrument is used, this parameter absorbs σ_X)	]-∞,∞[
γ_X	[km/s]	$\mathcal{U}$	Constant velocity offset of instrument X	]-∞,∞[
lin	[m s^{-1} yr^{-1}]	$\mathcal{U}$	Linear drift	]-∞,∞[
$\log(P)$	log([days])	$\mathcal{U}$	Logarithm of the period	[0,∞[
$\log(K)$	log([m s^{-1}])	$\mathcal{U}$	Logarithm of the RV semi-amplitude	[0,∞[
$\sqrt{e}\cos\omega$	-	$\mathcal{U}$		]-1,1[
$\sqrt{e}\sin\omega$	-	$\mathcal{U}$		]-1,1[
$\lambda_0 = M_0 + \omega$	[deg]	$\mathcal{U}$	Mean longitude (M_0 = mean anomaly)	[0,360[
Parameters probed by MCMC with magnetic cycle (in addition to the previous ones, except $\sigma_{JIT\,LOW}$ and $\sigma_{JIT\,HIGH}$ that replace σ_{JIT}				
$\sigma_{JIT\,LOW}$	[m s^{-1}]	$\mathcal{U}$	stellar jitter at the minimum of the magnetic cycle (If only one instrument is used, this parameter absorbs σ_X)	]-∞,∞[
$\sigma_{JIT\,HIGH}$	[m s^{-1}]	$\mathcal{U}$	stellar jitter at the maximum of the magnetic cycle (If only one instrument is used, this parameter absorbs σ_X)	]-∞,∞[
$\log(R'_{HK})\,lin$	[m s^{-1} $\log(R'_{HK})^{-1}$]	$\mathcal{U}$	slope of the correlation between the RV and $\log(R'_{HK})$ (The $\log(R'_{HK})$ variation is normalized between 0 and 1, thus this parameter is in [m s^{-1}])	]-∞,∞[
Physical Parameters derived from the MCMC posteriors (not probed)				
P	[d]	-	Period	
K	[m s^{-1}]	-	RV semi-amplitude	
e	-	-	Orbit eccentricity	
ω	[deg]	-	Argument of periastron	
T_P	[d]	-	Time of passage at periastron	
T_C	[d]	-	Time of transit	
Ar	[AU]	-	Semi-major axis of the relative orbit	
M.sin i	[M_{Jup}]	-	Mass relative to Jupiter	
M.sin i	[M_{Earth}]	-	Mass relative the Earth	

plerian orbital solution to the signal presenting the smallest p-value following the approach of Delisle et al. (2016) with the detected period as a guess value.
– Additional planets in the systems are then considered if other significant signals are present in the GLS periodogram of the RV residuals. Note that each time a Keplerian signal is added to the model, a global fit including all the previously detected signals is performed.
– We stopped when no more signals in the residuals present a p-value smaller than 1 % and we finally visually inspected the solutions.

4.3. Origin of the different signals found

After the main periodic signals have been recognized in the data, it is important to identify the ones that are very likely not from planetary origin. They may be of different natures: stellar, instrumental or observational. Here is a brief description of some cases encountered:

– *Stellar origin.* The signal is due to stellar intrinsic phenomena. The most common one is the variation of the measured RVs due to spectral line asymmetries induced by spots and faculae coming in and out of view of the surface of the star, modulating the signal over a star rotational period (Haywood et al. 2016, 2014; Dumusque et al. 2014a; Meunier et al. 2010; Desort et al. 2007; Saar & Donahue 1997). In order to spot RV variations of intrinsic stellar origin, we compare the periods of the derived orbital solutions with the rotational periods of the stars and their harmonics estimated using the $\log(R'_{HK})$ average activity level (see Table 1 Mamajek & Hillenbrand 2008; Noyes et al. 1984). We also compare the orbital periods with the variation timescales of spectroscopic activity indicators derived from the CCF, such as the BIS and the FWHM, and derived from spectral lines sensitive to activity, such as the the Ca II H and K lines (S-index and $\log(R'_{HK})$) or the Hα line (Hα-index).
– *Instrumental origin.* Spurious signals of small amplitudes with periods close to one year or an harmonic of it (half a year, a third of a year) can be created by a discontinuity in the wavelength calibration introduced by the stitching of the detector. The 4k×4k HARPS CCD is composed of 32 blocks of 512×1024 pixels. When each block were imprinted to form the detector mosaic, the technology at the time was not precise enough to ensure that pixels between blocks had the same size than intra-pixels. Therefore, every 512 pixels in the spectral direction, the CCD presents pixels that differs in size (Wilken et al. 2010). Block stitching may introduce a residual signal in the RVs at periods close to 6 months or 1 year when strong stellar lines crosse block stitchings due to the yearly motion of the Earth around the Sun. To avoid this effect, new sets of RVs for the stars presented in this paper

mation models. Signals of less significance are of course of great interest but require more observations to be confirmed as *bona fide* planets.

have been obtained by removing, from the used correlation masks, potentially affected spectral lines. For each star, the systemic velocity will shift the stellar spectrum on the CCD, therefore an optimization of the correlation mask is done on a star-by-star basis (for more information, see Dumusque et al. 2015).
– *Observational limitations.* Aliases have to be taken into account. The ones due to one year or one day sampling effects are well known (Dawson & Fabrycky 2010). They apply on all signals and not only on the planetary ones.

5. Description and analysis of individual systems

In this section, we present eight planetary systems including Neptune-mass and super-Earth planets. Presence of planets around these stars and preliminary system characterizations have been announced at the "Extreme Solar System II" conference held at Grand Teton USA in September 2011 and published in Mayor et al. (2011). We present here the detailed analysis of each system with updated data, describing and discussing the planetary system characteristics, as well as spurious (i.e. non-planetary) signals in the data.

5.1. HD 20003: Two Neptune-mass close-in eccentric planets close to the 3:1 commensurability

An ensemble of 184 high signal-to-noise observations (<S/N> of 110 at 550 nm) of HD 20003 have been gathered covering about 11 years (4063 days). The typical photon-noise plus calibration uncertainty of the observations is 0.74 ms^{-1}, well below the observed dispersion of the RVs at 5.35 $m\,s^{-1}$. The RVs with their GLS periodogram and the $\log(R'_{HK})$ time-series are displayed in Fig. 1. A long-period variation is observed in the RV data as well as in $\log(R'_{HK})$, indicative of a magnetic cycle effect on the velocities. To correct the velocities, we modeled the long-term variation by a Keplerian with parameters fixed and determined from the $\log(R'_{HK})$, except for the amplitude that was free to vary.

After correction for the long-period variation due to the magnetic cycle plus fitting a second-order polynomial drift, two peaks very clearly emerge well above the 0.1% p-value limit, at periods around 11.9 and 33.9 days (Fig. 2). Once those two signals are fitted for along with the magnetic cycle and the second-order polynomial drift, a significant signal at 184 days appears in the GLS periodogram of the RV residuals, with strong aliases at 127 and 359 days. A global fit including a second-order polynomial drift, a Keplerian for the magnetic cycle and three Keplerian for signals at 11.9, 33.9 and 184 days allows to model all the variations seen in the RVs, and no signal with p-values smaller than 5% are present in the RV residuals (Fig. 2, bottom-right plot).

After this preliminary phase looking for significant signals in the data, we searched for the best-fit parameters with an MCMC, using a model composed of a second-order polynomial drift, a linear correlation with $\log(R'_{HK})$ to adjust the magnetic cycle effect, three Keplerians to fit for the signals at 11.9, 33.9 and 184 days, two jitters that correspond to the instrumental plus stellar noise at the minimum and maximum of the magnetic cycle (see Sec. 4). This model converged to a stable solution, however, a significant signal in the residuals, shown in Fig. 3, was present near 3000 days, a period similar to that of the magnetic cycle. We tried to include an extra planet at this period in the system, but the MCMC did not converge to a solution where this signal disappeared. We found that there was a strong correlation between the linear fit to the RV-$\log(R'_{HK})$ correlation and either the second-order polynomial drift to the RVs or this extra Keplerian. This was therefore preventing the MCMC to converge to a correct solution. We therefore decided, as in the step-by-step approach, to fix the RV variation induced by the magnetic cycle by first fitting it in the $\log(R'_{HK})$ and then including this model to the RV fit with only the amplitude as a free parameter. On top of this model to fit the magnetic cycle, we added three Keplerians to fit for the signals at 11.9, 33.9 and 184 days, a second order polynomial, and one jitter corresponding to the instrumental plus stellar noise. In this case, the GLS periodogram of the residuals is extremely similar to the last plot in Fig. 2 and therefore no more signal is present in those RV residuals. We therefore adopt this solution as final, and note that in this system, an extra long-period planet not yet covered by our data might be present.

A surprising aspect of this system is the high eccentricity of the inner planet, e=0.38, while the planet at 33.9 days has an eccentricity close to 0. From a dynamical point of view, this is difficult to explain and a possibility is that the high eccentricity of the planet at 11.9 days hides a planet at half the orbital period (Anglada-Escudé et al. 2010). We therefore tried to fit a model with an extra planet with initial period at 5.95 days, fixing the eccentricities of the 5.95 and 11.9-day planets at zero and letting them free to vary. In both cases, the more complex solution is disfavored with a ΔBIC of 8.3 and 24.3, respectively. It seems therefore that the eccentricity of planet b is real. This can probably be explained by the fact that the two planet are close to a 3:1 commensurability with periods of 11.9 and 33.9 days. It is possible that in the past, the two planets were in resonance, which might have increase the eccentricity of the inner planet, and then a specific event made the two planet go slightly out of resonance on the nowadays orbit. Possible scenarios for this event could be instability when the gaz disappeared or the presence of an additional planet that was ejected when the eccentricity increased.

The best-fit for each planet, the signal at 184 days, and the RV residuals are displayed in Fig. 4. The best-fit parameters can be found in Table 5. A careful look at the activity indicators, $\log(R'_{HK})$, BIS SPAN and FWHM, after removing the long-period signal induced by the stellar magnetic cycle, reveals no significant peaks that match the planetary signals found in our analysis (see Fig. A.1). We are therefore confident that those signals are not induced by stellar activity.

The correlation between the activity index $\log(R'_{HK})$ and the RV residuals when removing all the detected signals except the magnetic cycle effect can be seen in the left panel of Fig. 5. Note that this correlation is considered in the model we used to fit the RV data.

Although the signals at 11.9 and 33.9 days are clearly induced by planets orbiting around HD 20003, the signal at 184 days is more difficult to interpret as it is located at half a year, with strong aliases at 127 days and 359 days, nearly a year. As explained in Sec. 4.3, signals at a year or harmonics of it can be induced by a discontinuity in the wavelength calibration introduced by tiny gaps between the different quadrants of the detector. However, the RV data that we analyze here have been corrected for this effect following the work of Dumusque et al. (2015). This correction has been already applied to the RVs of several stars, an has always been successful in removing the spurious signal. The fact that the RV residuals after removing the two planets, the second-order polynomial drift and the effect of the magnetic cycle do not correlate with the barycentric Earth RV (BERV, see right panel of Fig. 5) disfavors the hypothesis that the 184-day signal is due to a discontinuity in the wavelength calibration introduced by tiny gaps between the different quadrants of the detector. We would therefore be inclined

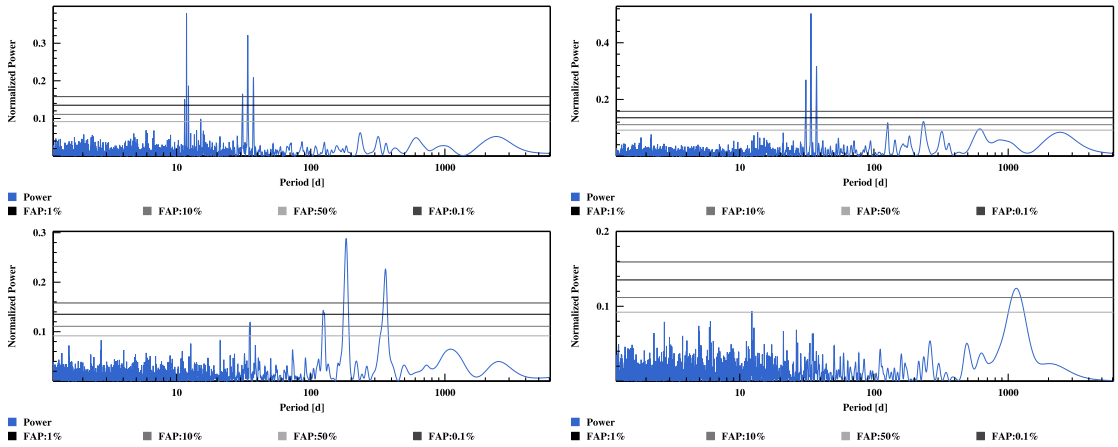

Fig. 2. GLS Periodogram of the RV residuals of HD 20003 at each step after removing, from left to right and then top to bottom, the magnetic cycle effect plus a second-order polynomial drift, then the two planets one after the other and finally the signal at 184 days. The GLS periodogram of the raw RVs is shown in Fig. 1.

Table 5. Best-fitted solution for the planetary system orbiting HD20003. For each parameter, the median of the posterior is considered, with error bars computed from the MCMC chains using a 68.3% confidence interval. σ_{O-C} corresponds to the weighted standard deviation of the residuals around this best solutions. All the parameters probe by the MCMC can be found in Annex, in Table B.1.

Param.	Units	HD20003b	HD20003c	HD20003d?	magn. cycle
P	[d]	$11.8496^{+0.0015}_{-0.0015}$	$33.8994^{+0.0239}_{-0.0215}$	$183.6129^{+1.0356}_{-1.0399}$	3297.7990 (fixed)
K	[m s^{-1}]	$3.82^{+0.21}_{-0.21}$	$3.19^{+0.19}_{-0.19}$	$1.59^{+0.20}_{-0.20}$	$5.13^{+0.48}_{-0.50}$
e		$0.38^{+0.05}_{-0.05}$	$0.06^{+0.06}_{-0.04}$	$0.13^{+0.11}_{-0.09}$	0.14 (fixed)
ω	[deg]	$-92.88^{+8.37}_{-8.26}$	$64.90^{+66.19}_{-53.48}$	$56.36^{+61.59}_{-59.53}$	-56.54 (fixed)
T_P	[d]	$55501.3634^{+0.2028}_{-0.2021}$	$55494.3925^{+6.3139}_{-5.0535}$	$55426.7488^{+29.4841}_{-29.3149}$	56732.7154 (fixed)
T_C	[d]	$55495.6321^{+0.3767}_{-0.3777}$	$55496.5959^{+0.6013}_{-0.7102}$	$55440.8098^{+5.2288}_{-5.6609}$	57986.4335 (fixed)
Ar	[AU]	$0.0973^{+0.0036}_{-0.0038}$	$0.1961^{+0.0072}_{-0.0077}$	$0.6048^{+0.0223}_{-0.0239}$	-
M.sin i	[M_{Jup}]	$0.0361^{+0.0034}_{-0.0032}$	$0.0462^{+0.0047}_{-0.0044}$	$0.0399^{+0.0060}_{-0.0058}$	-
M.sin i	[M_{Earth}]	$11.48^{+1.07}_{-1.03}$	$14.68^{+1.49}_{-1.41}$	$12.68^{+1.91}_{-1.83}$	-
γ_{HARPS}	[m s^{-1}]		$-16103.8822^{+0.4034}_{-0.4258}$		
$\sigma_{(O-C)}$	[m s^{-1}]		1.64		
log (Post)			$-363.9072^{+2.8436}_{-3.5486}$		

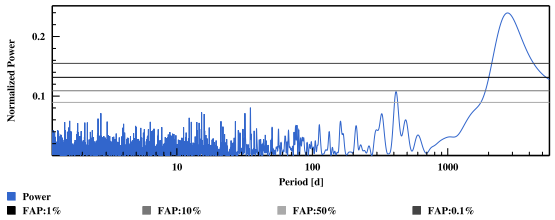

Fig. 3. GLS Periodogram of the RV residuals of HD 20003 obtained from the MCMC solution including a linear correlation between RV and $\log(R'_{HK})$ to account for the magnetic cycle, a second-order polynomial drift and three Keplerian.

to claim that this signal at 184 days is a real planetary signal. However, although intensively tested, there is still some possibilities that the data reduction system does not correct for all the instrumental effects in this particular case. We leave the signal as a potential one, and encourage other teams to confirm it using other pipelines or other facilities than HARPS.

The two Neptune mass planets found orbiting HD20003 are close to a 3:1 commensurability with periods of 11.9 and 33.9 days. This is probably the cause of the relatively high eccentricity of planet b.

5.2. HD 20781: A packed system with 2 super-Earths and 2 Neptune-mass planets

HD 20781 is part of a visual binary system including another star, HD 20782, known to host a planet on a 595-day very eccentric orbit (Jones et al. 2006). We take the opportunity of the discovery of a compact system of small planets around HD 20781 to provide here as well an updated solution for the planet around HD 20782 using HARPS data.

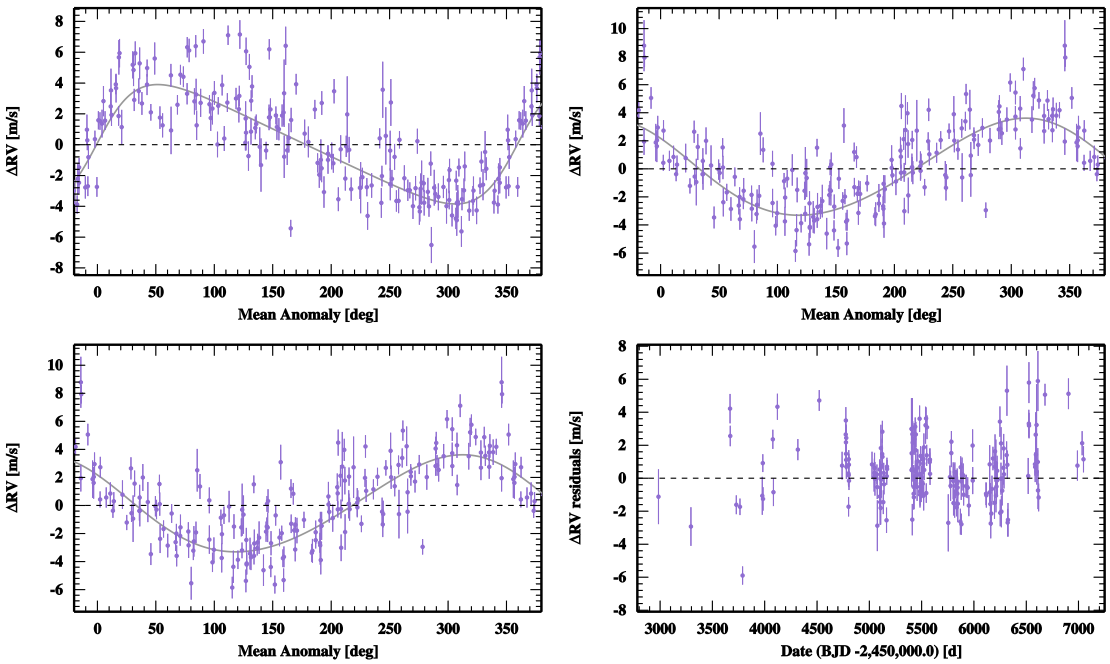

Fig. 4. Phase-folded RV measurements of HD 20003 with the best Keplerian solution represented as a black curve for each of the signals in the data. From top-left to bottom-right: planet b, planet c and the signal at 184 days. The residuals around the solution are displayed in the lower-right panel. Corresponding planetary orbital elements are listed in Table 5.

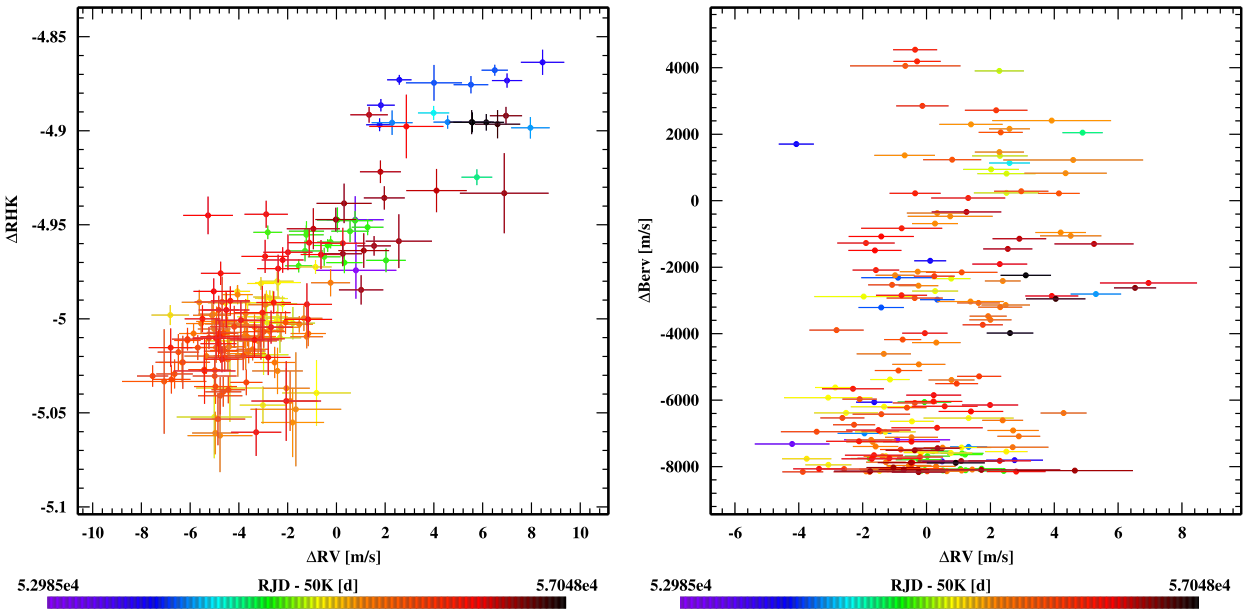

Fig. 5. *L*eft: Activity index $\log(R'_{HK})$ as a function of the RV residuals when removing all the detected signals except the magnetic cycle effect for HD 20003. The observed correlation indicates that most of the RV residual variation is due to activity-related effects. *R*ight: Barycentric Earth RV as a function of the RV residuals around the best derived solution without considering the 184-day signal. The fact that no correlation can be observed disfavor the hypothesis that the 184-day signal is due to a discontinuity in the wavelength calibration introduced by tiny gaps between the different quadrants of the detector.

HD 20781 was part of the original high-precision HARPS GTO survey and the star has been then followed for more than 11 years (4093 days). Over this time span, we gathered a total of 226 high signal-to-noise spectra (<S/N> of 112 at 550 nm) corresponding in the end to 216 RV measurements binned over 1 hour. As reported in Table 3, the typical precision of individual measurements is 0.76 m s^{-1}including photon noise and calibration uncertainties. The raw RV rms is significantly higher, at 3.41 m s^{-1}, pointing towards additional variations in the data of potentially stellar or planetary origin, assuming the instrumental effects are kept below the photon-noise level of the observations.

As a first approach we looked at the RV and activity index time series shown in Fig. 1. No significant long-term variation is observed in $\log(R'_{HK})$ data and no long-term variation is visible in the GLS periodogram of the velocity time series. We conclude that there is no noticeable sign of a magnetic activity cycle for

this star. The average value of $\log(R'_{HK})$ at -5.03 ± 0.01 is also very low with a very small dispersion, similar to the Sun at minimum activity. Checking at the periodograms of the $\log(R'_{HK})$, the BIS SPAN and the FWHM in Fig. A.2, we see that the $\log(R'_{HK})$ times series presents signals at 115, 81 and 68 days, and the FWHM time series at 380 days. This later signal is probably due to interaction with the window functions, creating a signal near a year, the former signals are however more difficult to interpret as they are not compatible with the estimated rotational period of the star, 35.2 days (see Table 1). Fitting the signal at 115 days removes the signal at 68 days, and the p-value of the signal at 81 days goes above 10%.

Due to the small activity level and the large number of observations, the GLS periodogram of the velocity series is very clean, with significant peaks clearly coming out of the noise background. So, even if the final characterization of the planetary system parameters is performed through a Bayesian-based MCMC approach, a step-by-step analysis of the system, characterizing and then removing one planet after the other from the data, will provide an excellent illustration of the significance of the planet detection in this system. The most prominent peak in the GLS periodogram is at a period around 20 days. Deriving a Keplerian solution for this planet and then removing the corresponding signal from the raw RVs makes a clear signal at 86 days appear in the GLS periodogram of the residuals (Fig. 6). Keeping on with the same approach, we can clearly identify, sequentially, significant signals first at 13.9 and then at 5.3 days. It has to be noted here that none of the significant periods in the data are close to the stellar rotational period, 46.8 days, estimated from the activity index (Table 1).

As described in Sec. 4, the final determination of the planetary system parameters is performed using a MCMC sampler and a model composed of four Keplerians representing the planetary signals, and an extra white-noise jitter to consider potential stellar or instrumental noise not included in the RV error bars (the σ_{JIT} parameter, see Table 4). Phase-folded planetary solutions, as well as the RV residuals around the best solution, are displayed in Fig. 7. The best-fit parameters are reported in Table 6. Checking in Fig. A.2 if any announced planet matches any signal in the activity indicators, we see that the 86-day Neptune-mass planet is close to the detected peaks in the $\log(R'_{HK})$ time-series at 115, 81 and 68 days. The amplitude of these signals is ∼0.01 dex, 20 times smaller than the solar magnetic cycle variation. Such signals can therefore not be responsible for the 2.6 $m\,s^{-1}$ periodic variation detected in the RVs at 86 days. In addition, fitting the 115-day signal removes all power at 68 and 81 days, therefore we are confident that the 86-day signal detected in the RVs is associated to the presence of a Neptune-mass planet orbiting HD 20781.

The system HD 20781 hosts two inner super-Earths with periods of 5.3 and 13.9 days and two outer Neptune-mass planets with periods of 29 and 86 days.

HD 20781 – HD 20782: More planets in this visual binary system

The star HD 20782 is the brightest companion of the HD 20781-HD 20782 binary system. It is known to harbor a 595-day very eccentric Jupiter planet (Jones et al. 2006). A total of 71 high signal-to-noise spectra (<S/N> of 181 at 550 nm) were obtained with HARPS on this target, which translates to 68 RV measurements after binning the data over 1 hour. Because of the very large semi-amplitude and eccentricity of the RV signal induced by the planet, we decided to include in addition to HARPS very precise measurements, the lower precision RV data obtained with UCLES (published in Jones et al. 2006) and CORALIE.

We searched for the best-fit parameters using a MCMC sampler. The solution converges to an extremely eccentric Jupiter-mass planet with a period of nearly 600 days. The phase-folded planetary solution, as well as the RV residuals around the best solution and their GLS periodogram, are displayed in Fig. 8. The best-fit parameters are reported in Table 6. Although the eccentricity, the amplitude and the argument of periastron are compatible within one sigma with the values presented in Jones et al. (2006), the period and argument of periastron are not compatible, even if different by less than 2%. This can be explained by the addition of CORALIE and HARPS data that allows to sample much better the periastron passage.

5.3. HD 21693: A system of 2 Neptune-mass planets close to a 5:2 resonance

Over a time span of 11 years (4106 days), 212 high signal-to-noise spectra (<S/N> of 141 at 550 nm) of HD 21693 were gathered, resulting in a total of 210 RV measurements when binning the data over 1 hour. The typical photon-noise and calibration uncertainty is 0.60 $m\,s^{-1}$, which is significantly below the 4.72 $m\,s^{-1}$ observed dispersion of the RVs, pointing towards the existence of additional signals in the data. The raw RVs, their GLS periodogram and the calcium activity index of HD 21693 are shown in Fig. 1. As we can see, the calcium activity index highlights a significant magnetic cycle with a variation in $\log(R'_{HK})$ ranging from -5.02 to -4.83. This magnetic cycle is extremely similar in magnitude to that of the Sun, however slightly shorter with a period of 10 years. When fitting a Keplerian signal to $\log(R'_{HK})$, we are left with significant signals at 740 and 33.5 days in the residuals (see Fig. A.3). Those signals are also present in the FWHM and the bisector span of the CCF, although less significant. The signal at ∼740 days, close to two years, is probably due to the sampling of the data, and the 33.5-day signal is likely the stellar rotation period. This value is compatible with the rotation period derived from the mean activity $\log(R'_{HK})$ level, i.e. 36 days (see Table 1).

Looking at the raw RVs and their GLS periodogram in Fig. 1, it is clear that the observed magnetic cycle has an impact on the measured RV measurements. To remove the RV contribution of the magnetic cycle, we remove from the RVs a Keplerian that has the same parameters as the Keplerian fitted to $\log(R'_{HK})$, with the exception that the amplitude is free to vary. The GLS periodogram of the RV residuals after correcting for the magnetic cycle effect are displayed in the top panel of Fig. 9. A highly significant signal at 54 days is present in the data. When removing this signal by fitting a Keplerian, an extra signal at 23 days is seen in the residuals (middle panel of Fig. 9). No signal with p-value smaller than 1% appears in the residuals of a two-Keplerian model; we therefore stop here looking for extra signals. Note however that the most significant signal left in the GLS periodogram corresponds to a period of 16 days, likely the first harmonic of the stellar rotation period, which is expected from stellar activity (Boisse et al. 2011).

After this preliminary phase looking for significant signal in the data, we search for the best-fit parameters with an MCMC, using a model composed of a linear correlation with $\log(R'_{HK})$ to adjust the magnetic cycle effect, two Keplerians to fit for the signals at 23 and 54 days, and two jitters that correspond to the instrumental plus stellar noise at the minimum and maximum of the magnetic cycle (see Sec. 4). The best-fit for each planet and the RV residuals are displayed in Fig. 10, and the best-fit

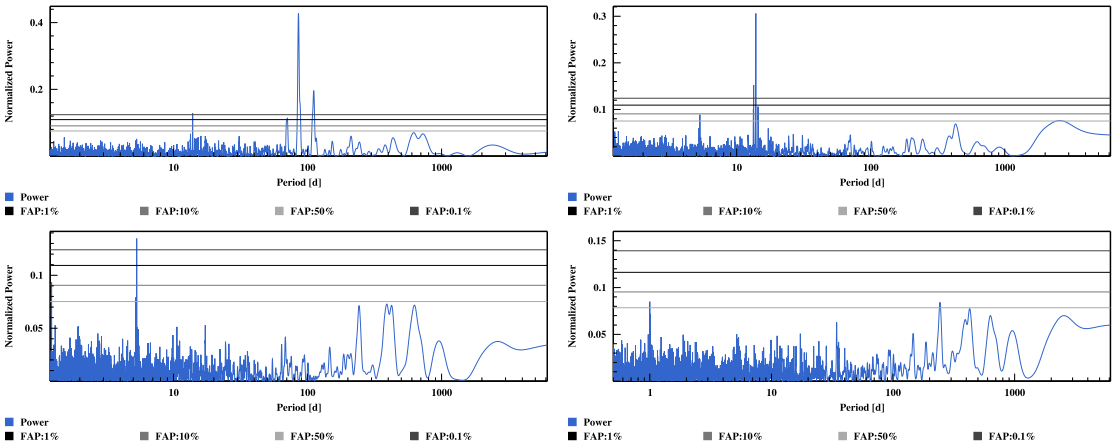

Fig. 6. GLS periodogram of the residuals at each step, after removing one planet after the other in the analysis of HD 20781 (from left to right and top to bottom). The GLS periodogram of the raw RVs is shown in Fig. 1.

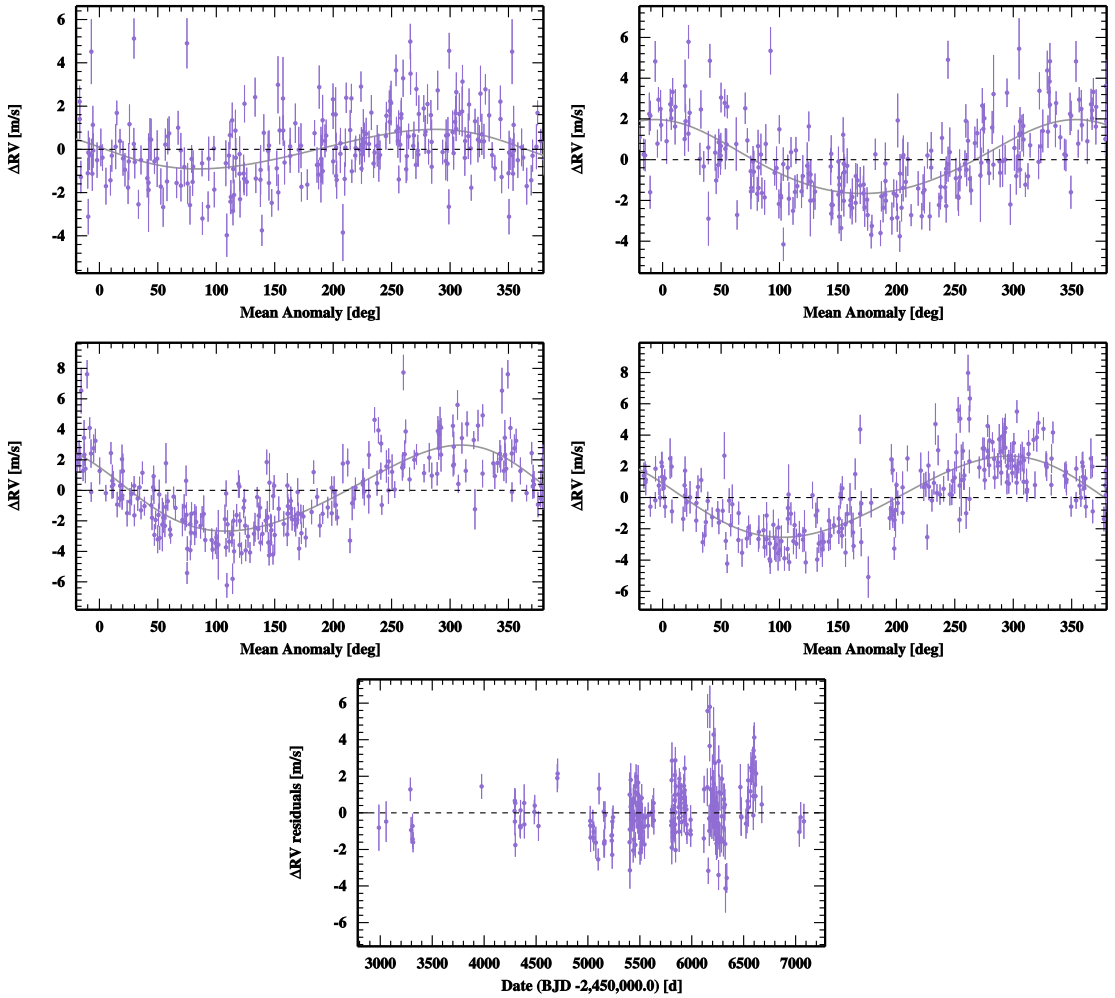

Fig. 7. Phase-folded RV measurements of HD 20781 with the best-fit solution represented as a black curve for each of the signal found in the data (from left to right and top to bottom: planet b, c, d and e). The residuals around the solution are displayed in the lower panel. Corresponding orbital elements are listed in Table 6.

parameters can be found in Table 7. None of the two detected planet corresponds to signals found in the activity indicators (see Fig. A.3).

When looking at the RV residuals, the scatter is still rather high even after removing all the significant signal detected in the data. Although in Hipparcos the star is catalogued as a G8 dwarf, the spectroscopic survey of nearby stars NSTAR finds that that HD 21693 is a G9IV-V therefore a slightly evolved star (Gray et al. 2006). Evolved stars presents higher photometric and RV jitter associated with more significant granulation, which might explain this significant residual jitter (Bastien et al. 2014, 2013; Dumusque et al. 2011d).

Table 6. Best-fitted solution for the planetary system orbiting HD20781 and HD20782. For each parameter, the median of the posterior is considered, with error bars computed from the MCMC posteriors using a 68.3% confidence interval. The value $\sigma_{(O-C)}$ corresponds to the weighted standard deviation of the residuals around this best solutions. All the parameters probed by the MCMC can be found in Annex, in Tables B.2 and B.3. See Table 4 for definition of the parameters.

Param.	Units	HD20781b	HD20781c	HD20781d	HD20781e	HD20782b
P	[d]	$5.3135^{+0.0010}_{-0.0010}$	$13.8905^{+0.0033}_{-0.0034}$	$29.1580^{+0.0102}_{-0.0100}$	$85.5073^{+0.0983}_{-0.0947}$	$597.0643^{+0.0256}_{-0.0256}$
K	[m s^{-1}]	$0.91^{+0.15}_{-0.15}$	$1.81^{+0.16}_{-0.16}$	$2.82^{+0.17}_{-0.16}$	$2.60^{+0.14}_{-0.14}$	$118.43^{+1.78}_{-1.78}$
e		$0.10^{+0.11}_{-0.07}$	$0.09^{+0.09}_{-0.06}$	$0.11^{+0.05}_{-0.06}$	$0.06^{+0.06}_{-0.04}$	$0.95^{+0.001}_{-0.001}$
ω	[deg]	$84.04^{+141.70}_{-108.41}$	$7.44^{+53.87}_{-70.21}$	$60.99^{+30.79}_{-30.03}$	$70.59^{+61.40}_{-67.58}$	$143.58^{+0.56}_{-0.66}$
T_P	[d]	$55503.2027^{+2.0979}_{-1.5934}$	$55503.5204^{+2.0425}_{-2.6815}$	$55511.3258^{+2.4394}_{-2.4382}$	$55513.3912^{+14.3623}_{-16.0090}$	$55247.0150^{+0.0770}_{-0.0837}$
T_C	[d]	$55503.2888^{+0.2361}_{-0.2384}$	$55506.4386^{+0.3546}_{-0.4385}$	$55513.2432^{+0.4250}_{-0.4410}$	$55517.4714^{+1.3596}_{-1.4838}$	$55246.1712^{+0.0706}_{-0.0706}$
Ar	[AU]	$0.0529^{+0.0024}_{-0.0027}$	$0.1004^{+0.0046}_{-0.0051}$	$0.1647^{+0.0076}_{-0.0083}$	$0.3374^{+0.0155}_{-0.0170}$	$1.3649^{+0.0466}_{-0.0495}$
M.sin i	[M$_{\rm Jup}$]	$0.0061^{+0.0012}_{-0.0011}$	$0.0168^{+0.0022}_{-0.0021}$	$0.0334^{+0.0038}_{-0.0037}$	$0.0442^{+0.0049}_{-0.0049}$	$1.4878^{+0.1045}_{-0.1066}$
M.sin i	[M$_{\rm Earth}$]	$1.93^{+0.39}_{-0.36}$	$5.33^{+0.70}_{-0.67}$	$10.61^{+1.20}_{-1.19}$	$14.03^{+1.56}_{-1.56}$	$472.83^{+33.22}_{-33.88}$
offset$_{UCLES}$	[m s^{-1}]					$5.4431^{+0.9302}_{-0.9370}$
γ_{COR98}	[m s^{-1}]					$39928.1039^{+1.8747}_{-1.9160}$
γ_{COR07}	[m s^{-1}]					$39930.6146^{+2.0828}_{-2.1696}$
γ_{COR14}	[m s^{-1}]					$39956.5569^{+1.5850}_{-1.6638}$
γ_{HARPS}	[m s^{-1}]		$40369.2080^{+0.1147}_{-0.1104}$			$39964.8070^{+0.2193}_{-0.2275}$
$\sigma_{(O-C)}$	[m s^{-1}]		1.45			2.34
log (Post)			$-397.1395^{+3.0943}_{-3.8525}$			$-379.6596^{+2.6521}_{-3.2805}$

The correlation between the activity index log(R$'_{HK}$) and the RV residuals removing only the two-planet solution can be seen in Fig. 11. Note that this correlation is considered in the MCMC model we used to fit the RV data.

Our analysis of the HARPS RV measurements of HD 21693 finds strong evidence that 2 Neptune-mass planets orbit the star, with periods of 22.7 and 53.7 days. With such periods, this planetary system is close to a 5:2 resonance. However, for such a resonance, the inner planet should be at a period slightly longer than the resonance and not smaller like it is the case here. This is something interesting to investigate further for dynamical purpose.

5.4. HD 31527: A 3-Neptune system

In total, 257 high signal-to-noise spectra (<S/N> of 180 at 550 nm) of HD 31527 were gathered over a time span of 11 years (4135 days). This results in 245 observations of the star when data are binned over 1 hour. The 3.19 m s^{-1}observed dispersion of the RVs is much larger than the typical RV precision of 0.64 m s^{-1}, pointing again towards the existence of extra signals in the data. The raw RVs, their GLS periodogram and the calcium activity index of HD 31527 are shown in Fig. 1. The calcium activity index log(R$'_{HK}$) does not show any significant variation as a function of time, therefore we do not expect the RVs to be affected by long-period signals generally induced by magnetic cycles. The mean activity level of the star is equal to log(R$'_{HK}$)= −4.96, very close to solar minimum. The RVs should therefore be exempt of activity signal at the rotational period

Table 7. Best-fitted solution for the planetary system orbiting HD21693. For each parameter, the median of the posterior is considered, with error bars computed from the MCMC chains using a 68.3% confidence interval. σ_{O-C} corresponds to the weighted standard deviation of the residuals around this best solutions. All the parameters probe by the MCMC can be found in Annex, in Table B.4.

Param.	Units	HD21693b	HD21693c
P	[d]	$22.6786^{+0.0085}_{-0.0087}$	$53.7357^{+0.0312}_{-0.0309}$
K	[m s^{-1}]	$2.20^{+0.22}_{-0.22}$	$3.44^{+0.20}_{-0.20}$
e		$0.12^{+0.09}_{-0.08}$	$0.07^{+0.06}_{-0.05}$
ω	[deg]	$-91.04^{+50.57}_{-50.35}$	$-17.34^{+47.50}_{-55.35}$
T_P	[d]	$55492.0549^{+3.0968}_{-3.1310}$	$55528.4064^{+7.0762}_{-8.1820}$
T_C	[d]	$55480.7554^{+0.7454}_{-0.6973}$	$55543.5822^{+1.0676}_{-1.2491}$
Ar	[AU]	$0.1455^{+0.0058}_{-0.0063}$	$0.2586^{+0.0103}_{-0.0113}$
M.sin i	[M$_{\rm Jup}$]	$0.0259^{+0.0034}_{-0.0033}$	$0.0547^{+0.0056}_{-0.0056}$
M.sin i	[M$_{\rm Earth}$]	$8.23^{+1.08}_{-1.05}$	$17.37^{+1.77}_{-1.79}$
γ_{HARPS}	[m s^{-1}]	$39768.8113^{+0.1425}_{-0.1471}$	
$\sigma_{(O-C)}$	[m s^{-1}]	2.05	
log (Post)		$-440.9160^{+2.2958}_{-3.1188}$	

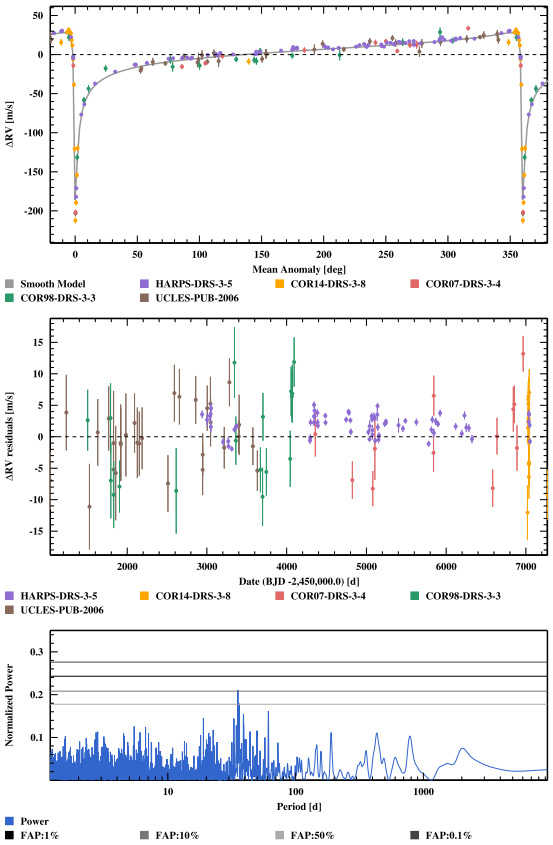

Fig. 8. Best keplerian solution for the eccentric planet orbiting HD 20782. *Top:* Phase-folded RV measurements with the best solution represented as a black curve. *Middle:* RV residuals around the best Keplerian solution. *Bottom:* GLS periodogram of the RV residuals. Corresponding orbital elements are listed in Table 6.

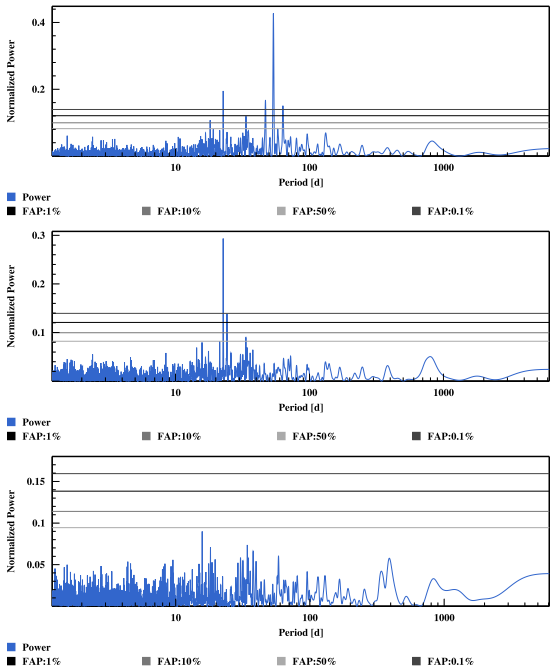

Fig. 9. *Top:* GLS periodogram of the residual RVs of HD 21693 after removing the RV contribution of the magnetic cycle. *Middle and bottom:* GLS periodogram of the residuals at each step, after removing one planet after the other in the analysis. The GLS periodogram of the raw RVs is shown in Fig. 1.

of the star and its harmonics due to active regions present on the stellar surface (Boisse et al. 2011). This is confirmed when looking at the periodograms of the different activity indicators in Fig. A.4. Only a signal at 400 days in the BIS SPAN is significant. This signal, close to a year, might be due the interaction between the time series and the window function.

As we can see in the GLS periodogram of the raw RVs (Fig. 1), two extremely significant signals appear at 17 and 52 days. After fitting these signals with a two-Keplerian model, a third significant signal at 271 days can be seen in the RV residuals (see middle panel of Fig. 12). The residuals of a three-Keplerian model do not show any signal with p-value smaller than 1%, therefore no extra signals seems to be present in the data (see bottom panel of Fig. 12). The fact that no signal is present at the estimated rotation period of the star (19 days, see Table 1) or its harmonics proves that the RVs of HD 31527 are not affected by significant activity signal.

After this first search for significant signals in the data, we fitted, using a MCMC sampler, a three-Keplerian model to the data including a white-noise jitter component to account for stellar and instrumental uncertainties not included in the RV error bars. The best-fit for each planet, as well as the RV residuals, can be seen in Fig. 13. We report in addition the best-fit parameters in Table 8.

None of the signals announced here matches signals in the different activity indicators (see Fig. A.4), therefore HD 31527 harbor 3 Neptune-mass planets, with periods of 16.6, 51.2 and 272 days. The star is a G2 dwarf like the Sun, therefore the outer planet in this system lies on an orbit between that of Venus and the Earth, therefore in the habitable zone of its host star (Selsis et al. 2007). This planet, with a minimum mass of 13 Earth-masses, is however likely composed of a large gas envelope (Rogers 2015; Wolfgang & Lopez 2015; Weiss & Marcy 2014), except if it is similar to Kepler-10c in composition (Dumusque et al. 2014b).

5.5. HD 45184: A system of two close-in Neptunes

We gathered a total of 309 high signal-to-noise spectra (<S/N> of 221 at 550 nm) of the G1.5 dwarf HD 45184 during a time span of 11 years (4160 days). This results in 178 RV measurements, when the data are binned over 1 hour, that exhibits an average precision of 0.41 $\mathrm{m\,s^{-1}}$considering photon noise and calibration uncertainties. The raw RV rms is much higher, 4.72 $\mathrm{m\,s^{-1}}$, which implies that significant signals are present in the data. In Fig. 1, we display the raw RVs and their GLS periodogram, and the $\log(R'_{HK})$ time series. We see that a significant magnetic cycle affects $\log(R'_{HK})$, with values ranging from -5.00 to -4.86 with a periodicity of 5 years. This magnetic cycle is therefore smaller in amplitude than that of the Sun, with a much shorter period. To see if significant signals were present in the calcium activity index despite the long-period magnetic cycle, we fitted the $\log(R'_{HK})$ time series with a Keplerian. In the residuals, a strong signal at 20 days is present, likely corresponding to the stellar rotation period (see Fig. A.5). This value is fully compatible with the rotation estimated using the $\log(R'_{HK})$ average level (19 days, see Table 1 and Mamajek & Hillenbrand 2008; Noyes et al. 1984).

Looking at the raw RVs of HD 45184 and their GLS periodogram in Fig. 1, we see that the magnetic cycle observed in $\log(R'_{HK})$ has an influence on the RVs. To remove the RV contribution of the magnetic cycle, we fitted the $\log(R'_{HK})$ with a Kep-

Table 8. Best-fitted solution for the planetary system orbiting HD31527. For each parameter, the median of the posterior is considered, with error bars computed from the MCMC chains using a 68.3% confidence interval. σ_{O-C} corresponds to the weighted standard deviation of the residuals around this best solutions. All the parameters probe by the MCMC can be found in Annex, in Table B.5.

Param.	Units	HD31527b	HD31527c	HD31527d
P	[d]	$16.5535^{+0.0034}_{-0.0035}$	$51.2053^{+0.0373}_{-0.0368}$	$271.6737^{+2.1135}_{-2.2471}$
K	[m s^{-1}]	$2.72^{+0.13}_{-0.13}$	$2.51^{+0.14}_{-0.14}$	$1.25^{+0.17}_{-0.16}$
e		$0.10^{+0.05}_{-0.05}$	$0.04^{+0.05}_{-0.03}$	$0.24^{+0.13}_{-0.13}$
ω	[deg]	$41.12^{+29.46}_{-34.41}$	$-23.25^{+68.94}_{-152.43}$	$179.00^{+31.11}_{-26.20}$
T_P	[d]	$55499.5453^{+1.3130}_{-1.5818}$	$55526.3434^{+9.7876}_{-21.5943}$	$55718.8091^{+21.3880}_{-17.3759}$
T_C	[d]	$55501.4585^{+0.2640}_{-0.2667}$	$55542.0635^{+0.7471}_{-0.9373}$	$55670.8324^{+11.7715}_{-13.7509}$
Ar	[AU]	$0.1254^{+0.0041}_{-0.0045}$	$0.2663^{+0.0088}_{-0.0095}$	$0.8098^{+0.0273}_{-0.0293}$
M.sin i	[M_{Jup}]	$0.0329^{+0.0028}_{-0.0028}$	$0.0445^{+0.0040}_{-0.0039}$	$0.0372^{+0.0053}_{-0.0052}$
M.sin i	[M_{Earth}]	$10.47^{+0.89}_{-0.87}$	$14.16^{+1.28}_{-1.23}$	$11.82^{+1.70}_{-1.64}$
γ_{HARPS}	[m s^{-1}]		$25739.7025^{+0.0952}_{-0.0971}$	
$\sigma_{(O-C)}$	[m s^{-1}]		1.41	
log (Post)			$-439.4138^{+2.7350}_{-3.3929}$	

lerian, and removed the same Keplerian from the RVs leaving the amplitude as a free parameter. In the residuals, displayed in the top panel of Fig. 14, we see a significant signal at 6 days. Once this signal is removed by fitting a Keplerian with the guessed period, another signal at 13 days appears (see middle panel of Fig. 14). Finally after removing a two-Keplerian model to the RVs corrected for the magnetic cycle effect, no signal with p-value smaller than 10% appear. We therefore stop here looking for extra signals in the data. Note that although not significant, the highest peak in the GLS periodogram of the RV residuals is at 18.6 days, likely the imprint of the stellar rotation period, estimated to be 21.5±3.0 from the log(R'_{HK}) mean level (see Table 4). The RVs are therefore slightly affected by stellar activity, however at a level that is not perturbing the detection of the two planets at 6 and 13 days.

After the preliminary phase of looking for significant signals, we fitted the RVs using a MCMC sampler and a model composed of a linear correlation with log(R'_{HK}) to adjust the magnetic cycle effect, two Keplerians to fit for the signals at 5.9 and 13.1 days, and two jitters that correspond to the instrumental plus stellar noise at the minimum and maximum of the magnetic cycle (see Sec. 4). Each planet with its best-fit can be seen in Fig. 15, as well as the RV residuals after the best-fit has been removed. The best-fit parameters are reported in Table 9. None of the signals at 5.9 and 13.1 matched signals in the different activity indicators (see Fig. A.5), and therefore those signal are associated with *bona-fide* planets.

In Fig. 16, we show the RV residuals after removing the best-fit solution for planets b and c as a function of the log(R'_{HK}). The observed strong correlation indicates that most of the residuals are due to activity-related effects and motivates the use of our model that includes a linear fit between log(R'_{HK}) and RVs to mitigate the effect of long-term activity.

Our analysis of the HARPS RV measurements of HD 45184 shows that 2 Neptune-mass planets orbit close to the star, with periods of 5.9 and 13.1 days.

Table 9. Best-fitted solution for the planetary system orbiting HD45184. For each parameter, the median of the posterior is considered, with error bars computed from the MCMC chains using a 68.3% confidence interval. σ_{O-C} corresponds to the weighted standard deviation of the residuals around this best solutions. All the parameters probe by the MCMC can be found in Annex, in Table B.6.

Param.	Units	HD45184b	HD45184c
P	[d]	$5.8854^{+0.0003}_{-0.0003}$	$13.1354^{+0.0026}_{-0.0025}$
K	[m s^{-1}]	$4.26^{+0.23}_{-0.23}$	$2.36^{+0.23}_{-0.23}$
e		$0.07^{+0.05}_{-0.05}$	$0.07^{+0.07}_{-0.05}$
ω	[deg]	$145.80^{+49.43}_{-47.76}$	$-197.97^{+119.85}_{-80.87}$
T_P	[d]	$55500.2509^{+0.7996}_{-0.7790}$	$55497.4412^{+4.4543}_{-2.9188}$
T_C	[d]	$55499.4150^{+0.1050}_{-0.0903}$	$55494.8821^{+0.3364}_{-0.3065}$
Ar	[AU]	$0.0644^{+0.0020}_{-0.0021}$	$0.1100^{+0.0034}_{-0.0036}$
M.sin i	[M_{Jup}]	$0.0384^{+0.0033}_{-0.0032}$	$0.0277^{+0.0034}_{-0.0032}$
M.sin i	[M_{Earth}]	$12.19^{+1.06}_{-1.03}$	$8.81^{+1.09}_{-1.02}$
γ_{HARPS}	[m s^{-1}]	$-3757.6506^{+0.1562}_{-0.1595}$	
$\sigma_{(O-C)}$	[m s^{-1}]	2.15	
log (Post)		$-382.5338^{+2.3828}_{-2.9637}$	

5.6. HD 51608: 2 Neptune-mass planets

Over a time span of 11 years (4158 days), 218 high signal-to-noise spectra (<S/N> of 133 at 550 nm) of HD 51608 were gathered with HARPS, resulting in a total of 216 measurements binned over 1 hour with a typical photon-noise and calibration uncertainty of 0.62 m s^{-1}. This value is significantly below the

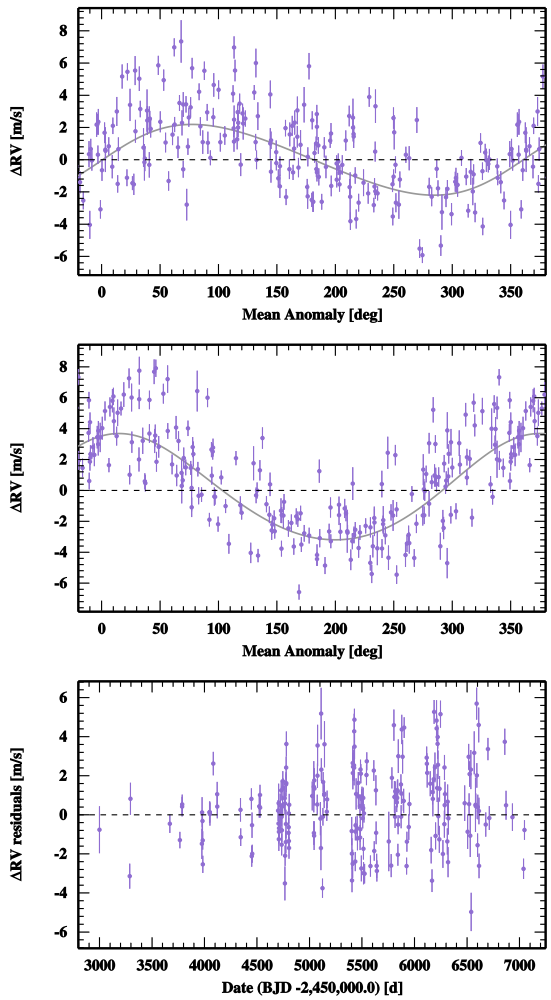

Fig. 10. Phase-folded RV measurements of HD 21693 with the best planet solution represented as a black curve for each of the signal in the data (top to bottom: planet b and planet c). The residuals around the solution are displayed in the lower panel. Corresponding orbital elements are listed in Table 7.

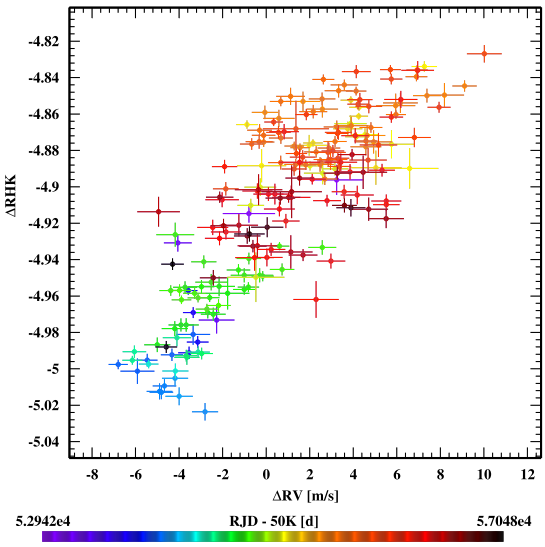

Fig. 11. RV residuals when removing all the detected signals except the magnetic cycle effect plotted as a function of the activity index $\log(R'_{HK})$ for HD 21693. The observed correlation indicates that most of the RV residual variation is due to activity-related effects.

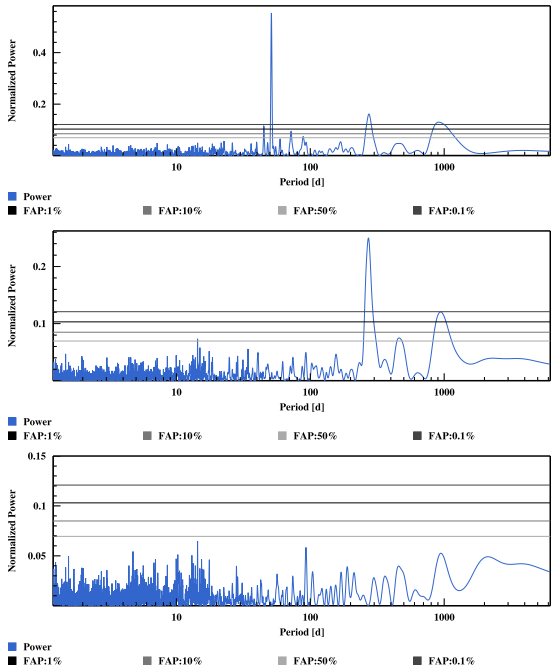

Fig. 12. *Top:* GLS periodogram of the residual RVs of HD 31527 after removing the best-fit Keplerian to account for the significant signal at 17 days seen in the raw RVs (bottom right panel of Fig. 1). *Middle and bottom:* GLS periodogram of the residuals at each step, after removing the second and third planet from the RVs.

4.07 m s^{-1}observed dispersion of the RV, pointing towards the existence of additional signals in the data. The raw RVs, their GLS periodogram and the calcium activity index of HD 51608 are shown in Fig. 1. A small, albeit significant, long-term variation can be seen in $\log(R'_{HK})$, with values in $\log(R'_{HK})$ ranging from -5.04 to -4.96 and with a period of 11 years. Although the period of this magnetic cycle is very similar to that of the Sun, its amplitude is much lower. After fitting this long-period signal in $\log(R'_{HK})$, a signal with a p-value of ~5% and a period of 37 days is detected in the $\log(R'_{HK})$ residuals, the BIS SPAN and the FWHM of the CCF (see Fig. A.6). This is likely a signature of stellar activity as the mean $\log(R'_{HK})$ level gives an estimated rotation period of 40±4 days (see Table 1 and Mamajek & Hillenbrand 2008; Noyes et al. 1984).

In the raw RVs, very strong signals at 14 and 96 days are present (see Fig. 1). Once fitting a two Keplerian model to account for those signals, a long-period signal with a p-value smaller than 0.1% appear in the GLS periodogram (see middle panel of Fig. 17). This signal is induced by the stellar magnetic cycle, and we remove it as in the precedent cases by fitting a Keplerian to the $\log(R'_{HK})$, and removing the same Keplerian from the RVs leaving the amplitude as a free parameter. After fitting the effect of the two planets plus the magnetic cycle, no significant signal with p-value smaller than 10% is left in the residuals.

After this preliminary stage of checking significant signal in the data, we searched for the best-fit parameters using a MCMC sampler, and selecting a model composed of a linear correlation with $\log(R'_{HK})$ to adjust the magnetic cycle effect, two Keplerians to fit for the signals at 14.1 and 96.0 days, and two jitters that correspond to the instrumental plus stellar noise at the minimum and maximum of the magnetic cycle (see Sec. 4). The best-fit

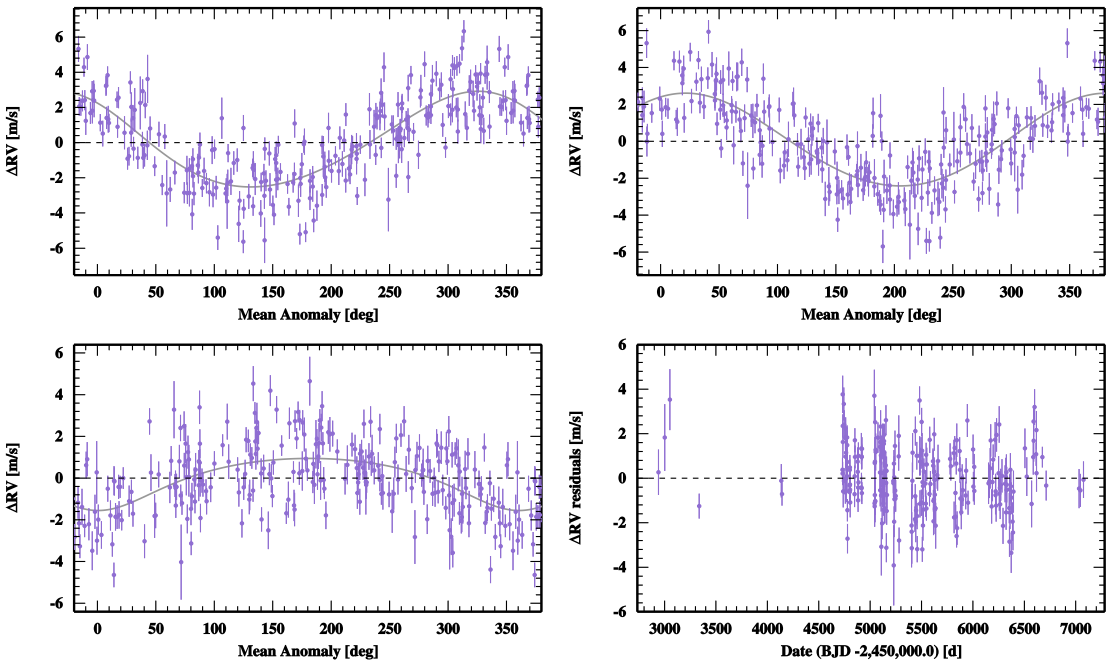

Fig. 13. Phase-folded RV measurements of HD 31527 with the best Keplerian solution for planet b, c, d and e represented as black curves (from left to right and top to bottom). The residuals around the solution are displayed in the bottom right panel. Corresponding orbital elements are listed in Table 8.

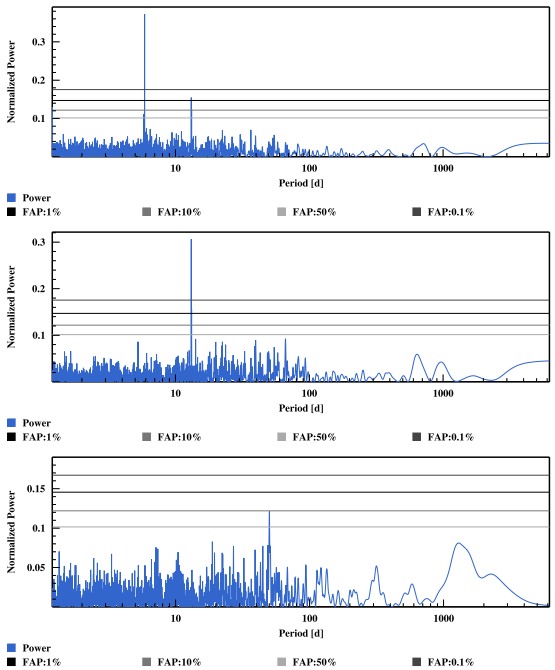

Fig. 14. From top to bottom: GLS periodogram of the RVs after removing the effect induced by the stellar magnetic cycles and then one planet after the other in the analysis of HD 45184. The GLS periodogram of the raw RVs is shown in Fig. 1.

solution for the two planets are shown in Table 10 and illustrated in Fig. 18, along with the RV residuals. The two signals detected in RVs are not matching any significant signal in the different activity indicators (see Fig. A.6) and are therefore associated to *bona-fide* planets.

The correlation between the activity index $\log(R'_{HK})$ and the RV residuals removing only the two-planet solution can be seen in Fig. 19. Note that this correlation is considered in the model we used to fit the RV data.

With planetary masses of 14.3 and 12.8 Earth-masses, HD 51608 harbors two Neptune-like planets, except if one of them is similar in composition to Kepler-10c (Dumusque et al. 2014b)

5.7. HD 134060: A short-period Neptune on an eccentric orbit with a long-period more massive companion

A total of 335 high signal-to-noise spectra (<S/N> of 199 at 550 nm) of HD 134060 have been gathered over a time span of 11 years (4083 days). When binning the measurements over one hour, we are left with 155 RV measurements, with a typical photon-noise plus calibration uncertainty of 0.40 m s^{-1}. This is an order of magnitude below the observed dispersion of the RVs, 3.68 m s^{-1}. The raw RV with the corresponding GLS periodogram and the $\log(R'_{HK})$ time series are displayed in Fig. 1. The $\log(R'_{HK})$ time series does not present any long-term trend and $\log(R'_{HK})$ varies between -5.05 and -5, which corresponds to an activity level similar to solar minimum. We therefore do not expect strong signals induced by stellar activity. This is confirmed by the fact that no significant signals appears in the periodogram of the different activity indicators in Fig. A.7.

One very significant signal at 3.3 days can be seen in the GLS periodogram of the raw RVs (see Fig. 1). Once this signal is fitted with a Keplerian, another significant peak appears at 1292 days, as can be seen in Fig. 20. After fitting simultaneously those two signals, nothing is left in the RV residuals with p-values smaller than 10%. We therefore stop there looking for extra signals.

To get the best possible orbital parameters for those two planets with reliable error bars, we perform an MCMC analysis with a model composed of two Keplerians plus a white-noise jitter to account for stellar and instrumental uncertainties not included in the RV error bars. The best-fit parameters can be found in Ta-

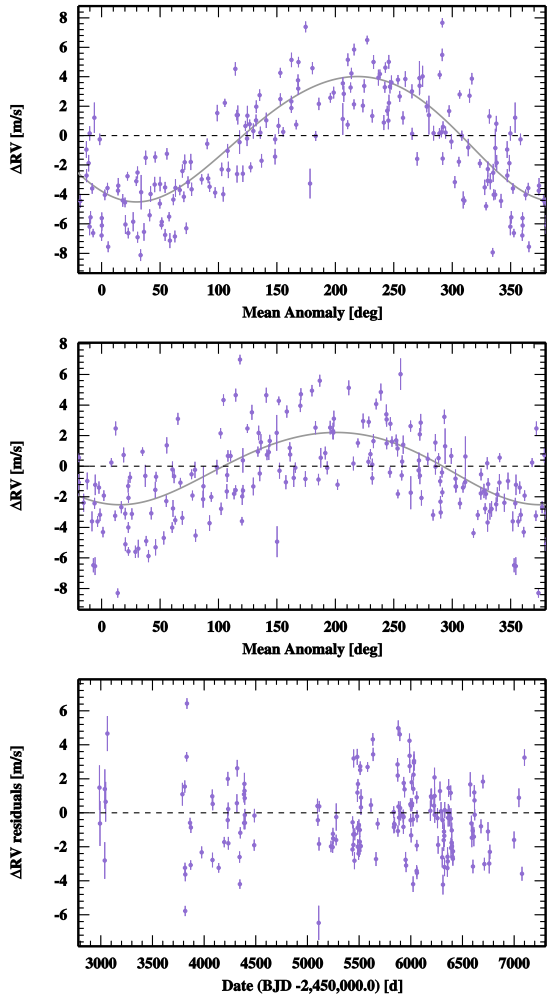

Fig. 15. Phase-folded RV measurements of HD 45184 with, from top to bottom the best Keplerian solution for planet b, c and the residuals around the best-fitted solution. Corresponding orbital elements are listed in Table 9.

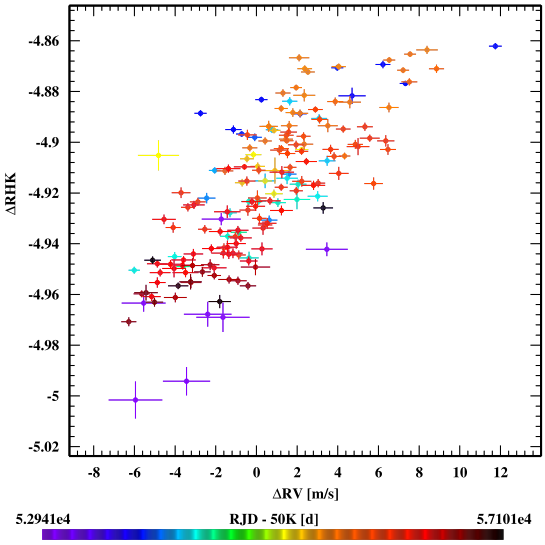

Fig. 16. RV residuals when removing all the detected signals except the magnetic cycle effect plotted as a function of the activity index $\log(R'_{HK})$ for HD 45184. The observed correlation indicates that most of the RV residual variation is due to activity-related effects.

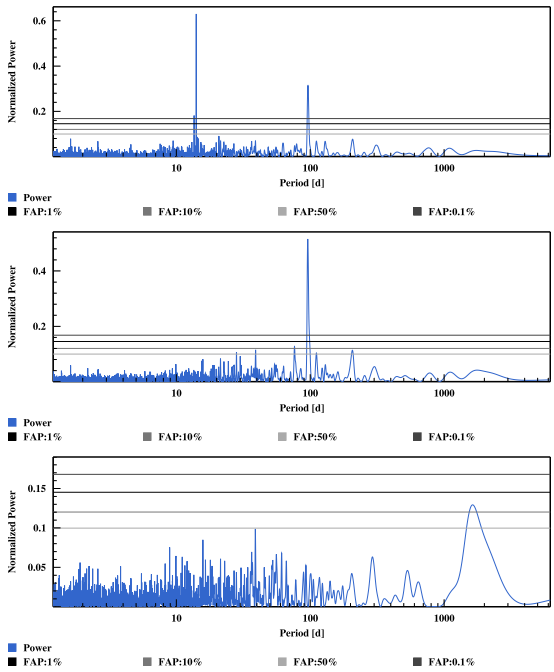

Fig. 17. From top to bottom: GLS periodogram of the RV residuals of HD 51608 after removing the effect of the magnetic cycle and at each step, after removing one planet after the other. The GLS periodogram of the raw RVs is shown in Fig. 1.

ble 11. The planetary signals, folded in phase, can be seen in Fig. 21 along with the RV residuals shown in the bottom plot.

The MCMC converges to a solution with an inner planet of minimum mass 10.1 $M_\oplus$ and period 3.27 days, on a relatively high eccentricity orbit, i.e. $e = 0.45$. This high eccentricity can hide a planetary system in 2:1 resonance, thus the existence of another planet at half its orbital period (Anglada-Escudé et al. 2010). We therefore tried to fit a model with an extra planet at 1.65 days, fixing the eccentricities at zero and leaving them free to vary. In both cases, the more complex solution is disfavored with a ΔBIC of 3.1 and 23.5, respectively. We therefore keep the simplest solution with the relatively high eccentricity of the inner planet. This planet has a long-period companion that has a minimum mass three times larger. It is therefore likely that this long-period planet is perturbing its inner companion through a Lidov-Kozai mechanism, causing libration of its orbit (Kozai 1962; Lidov 1961). During this process, the eccentricity of the inner planet can reach very high values. The inner planet therefore starts to interact with its host star during close fly-bys, implying a circularization of the inner planet's orbit on very short period orbits. Because of the conservation of the total angular momentum, eccentricity can increase only if the inclination of the orbit changes. Inner planets under the influence of a Lidov-Kozai mechanism should therefore be on inclined orbits relative to the stellar rotational plane. This can be measured using the Rossiter-McLaughlin effect if by chance the planet transits its host star. The difficulty here is that for a planet at 3.3 days, the circularization timescale is normally very short, therefore preventing of observing systems in such a configuration.

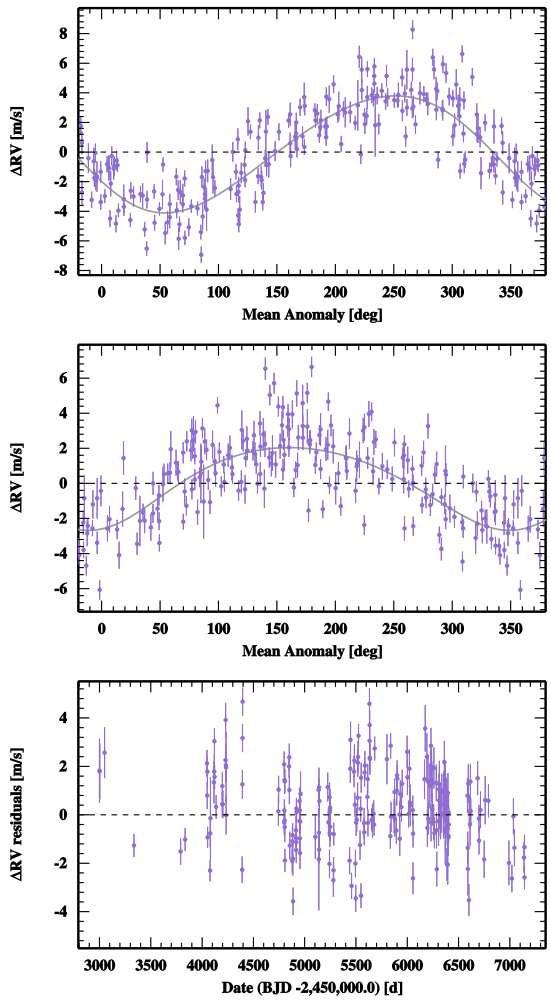

Fig. 18. Phase-folded RV measurements of HD 51608 with, from top to bottom the best Keplerian solution for planet b, c and the residuals around the best-fitted solution. Corresponding orbital elements are listed in Table 10.

5.8. HD 136352: A 3-planet system

HD 136352 was part of the original high-precision HARPS GTO survey and the star has been followed for nearly 11 years (3993 days). Over this time span, we gathered a total of 649 high signal-to-noise spectra (<S/N> of 231 at 550 nm) corresponding in the end to 240 RV measurements binned over 1 hour. As reported in Table 3, the typical precision of individual measurements is 0.33 m s^{-1}including photon noise and calibration uncertainties, an order of magnitude smaller than the observed raw RV rms, i.e. 2.74 m s^{-1}. This suggest that significant signals, of stellar or planetary origin, are present in the data. As a first approach we looked at the log(R'_{HK}) activity index time serie in Fig. 1. No significant long-term variation is observed in the log(R'_{HK}) data and no long-term variation is visible in the GLS periodogram of the velocity time series. We conclude that there is no noticeable sign of a magnetic activity cycle for this star. The average value of log(R'_{HK}) at −4.95 is low with a small dispersion of ∼ 0.01, close to the Sun at minimum activity. No significant effect of stellar activity in the RV measurements is thus expected for this star. This is confirmed by the fact that no significant signals appears in the periodogram of the different activity indicators in Fig. A.8.

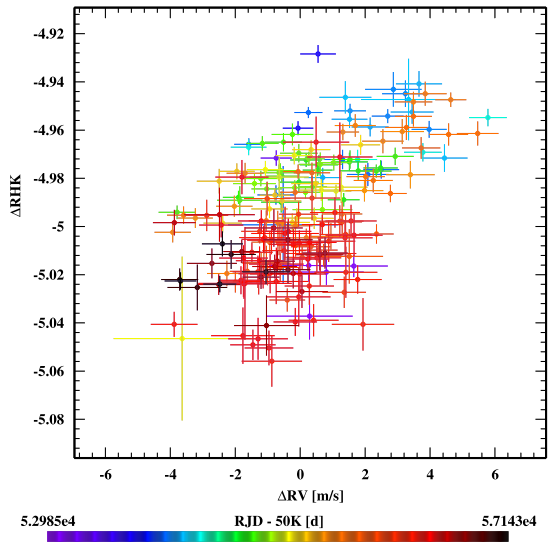

Fig. 19. RV residuals around the best derived solution without considering the magnetic cycle effect plotted as a function of the activity index log(R'_{HK}) for HD 51608. The observed correlation indicates that most of the RV residual variation is due to activity-related effects.

Table 10. Best-fitted solution for the planetary system orbiting HD51608. For each parameter, the median of the posterior is considered, with error bars computed from the MCMC chains using a 68.3% confidence interval. σ_{O-C} corresponds to the weighted standard deviation of the residuals around this best solutions. All the parameters probe by the MCMC can be found in Annex, in Table B.7.

Param.	Units	HD51608b	HD51608c
P	[d]	$14.0726^{+0.0016}_{-0.0016}$	$95.9446^{+0.1555}_{-0.1366}$
K	[m s^{-1}]	$3.95^{+0.16}_{-0.16}$	$2.36^{+0.17}_{-0.17}$
e		$0.09^{+0.04}_{-0.04}$	$0.14^{+0.07}_{-0.07}$
ω	[deg]	$117.45^{+30.27}_{-28.91}$	$-165.07^{+29.34}_{-33.93}$
T_P	[d]	$55494.5239^{+1.1795}_{-1.1073}$	$55498.3725^{+7.6262}_{-9.0495}$
T_C	[d]	$55493.6039^{+0.1684}_{-0.1646}$	$55474.0824^{+2.5542}_{-2.5650}$
Ar	[AU]	$0.1059^{+0.0043}_{-0.0046}$	$0.3809^{+0.0153}_{-0.0164}$
M.sin i	[M_{Jup}]	$0.0402^{+0.0038}_{-0.0037}$	$0.0450^{+0.0051}_{-0.0048}$
M.sin i	[M_{Earth}]	$12.77^{+1.20}_{-1.19}$	$14.31^{+1.63}_{-1.53}$
γ_{HARPS}	[m s^{-1}]	$39977.2351^{+0.1159}_{-0.1147}$	
$\sigma_{(O-C)}$	[m s^{-1}]	1.60	
log (Post)		$-409.1398^{+2.4423}_{-3.1572}$	

Due to the small activity level and the large number of observations, the GLS periodogram of the velocity series is actually very clean, with peaks at 27.6, 11.6 and 108 days, in order of decreasing significance (see Fig. 22). After fitting those three signals with Keplerians, a study of the GLS periodogram of the RV residuals shows a peaks at 123 days with a p-value between 1 and 0.1%, thus an interesting signal that we will consider in the MCMC analysis.

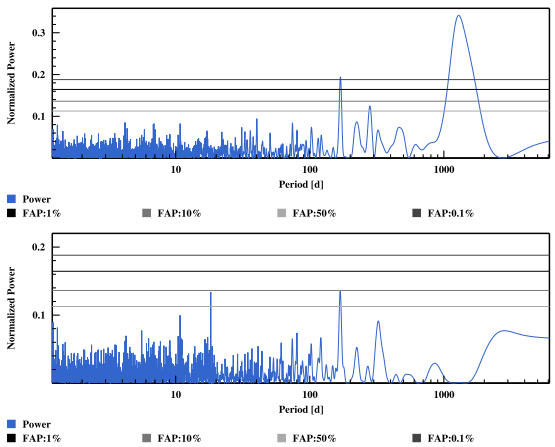

Fig. 20. From top to bottom: GLS periodogram of the residuals at each step, after removing one planet after the other in the analysis of HD 134060. The GLS periodogram of the raw RVs is shown in Fig. 1.

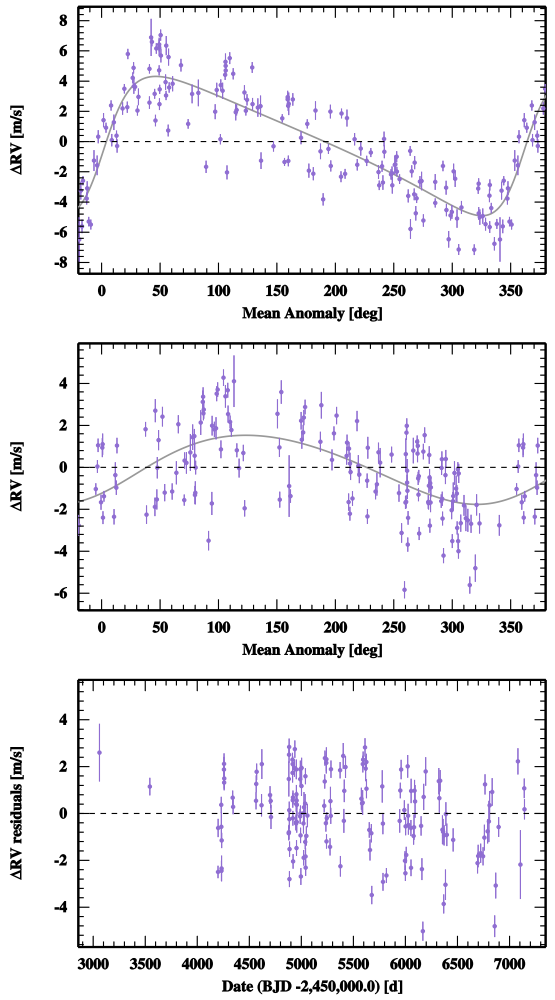

Fig. 21. Phase-folded RV measurements of HD 134060 with the best fitted solution for planet b and c represented as a black curve. The RV residuals around the best-fit solution are displayed in the lower panel. Corresponding orbital elements are listed in Table 11.

The best orbital parameters for the three planets orbiting HD 136352 are searched for using a MCMC sampler using a model composed of three Keplerians and an extra white-noise jitter to account for instrumental and stellar uncertainties not included in the RV error bars. Phase-folded planetary solutions are displayed in Fig. 23, as well as the RV residuals around the best solution. The best-fit parameters are reported in Table 12.

Table 11. Best-fitted solution for the planetary system orbiting HD134060. For each parameter, the median of the posterior is considered, with error bars computed from the MCMC posteriors using a 68.3% confidence interval. The value $\sigma_{(O-C)}$ corresponds to the weighted standard deviation of the residuals around this best solutions. All the parameters probed by the MCMC can be found in Annex, in Table B.8. See Table 4 for definition of the parameters.

Param.	Units	HD134060b	HD134060c
P	[d]	$3.2696^{+0.0001}_{-0.0001}$	$1291.5646^{+48.0333}_{-44.2197}$
K	[m s^{-1}]	$4.61^{+0.22}_{-0.22}$	$1.65^{+0.24}_{-0.23}$
e		$0.45^{+0.04}_{-0.04}$	$0.11^{+0.13}_{-0.07}$
ω	[deg]	$-98.23^{+6.61}_{-6.75}$	$-132.73^{+121.28}_{-55.51}$
T_P	[d]	$55499.6542^{+0.0420}_{-0.0407}$	$55232.8160^{+444.3209}_{-186.5492}$
T_C	[d]	$55498.1943^{+0.1065}_{-0.1037}$	$56057.2704^{+61.2663}_{-48.5676}$
Ar	[AU]	$0.0444^{+0.0013}_{-0.0014}$	$2.3928^{+0.0929}_{-0.0951}$
M.sin i	[M$_{\rm Jup}$]	$0.0318^{+0.0025}_{-0.0024}$	$0.0922^{+0.0139}_{-0.0133}$
M.sin i	[M$_{\rm Earth}$]	$10.10^{+0.79}_{-0.75}$	$29.29^{+4.43}_{-4.24}$
γ_{HARPS}	[m s^{-1}]	$37987.9484^{+0.1512}_{-0.1489}$	
$\sigma_{(O-C)}$	[m s^{-1}]	1.64	
log (Post)		$-304.2166^{+2.1293}_{-2.9181}$	

As said two paragraphs above, an interesting signal is present in the residuals at 123 days, and we ran another MCMC trial including this fourth signal. The fit converged towards a non-eccentric signal with an amplitude of 0.65 m s^{-1}and a period of 122.6 days. However, when comparing the three- and four-planet model solutions, the case with three planets is strongly favored, with a ΔBIC of 39.6. We also tried to add to the three-planet model a polynomial of the first or the second order to check if this 123-day signal could be due to a very-long period companion, whose orbit is not covered by the data, and therefore creates an alias at a period of a year or one of its harmonics. However this did not reduce the signal at 123 days and was disfavored by a model comparison using the BIC. We also looked for other possibilities of the three planet scenario, fitting the aliases of the 11 and 27.6-day signals, 0.91 and 0.96 day, respectively. These other possibilities are also ruled out with difference in BIC>17. Finally we tested the sensitivity of the GLS periodogram to outliers. We found that by simply removing two of them, for example JD 2455411 and 24556168, the amplitude of the peak found at 123 days goes above a p-value of 1%. Therefore a lot of arguments points in the direction that this interesting, albeit not conclusively significant signal at 123 days is more likely an artefact induced by noise in the data or interaction with the window function rather than a *bona-fide* planet. We therefore keep for HD 136352 the three planet solution, with periods of 11.6, 27.6 and 108 days.

Our analysis of HD 136352 converges to the detection of three planet orbiting this G4V star. With minimum masses of 4.8, 8.6 and 10.8 $M_\oplus$, HD 136352 host three super-Earth on orbits ranging from 11 to 108 days. The two inner planets, with periods of 11.6 and 27.6 days are close to a 5:2 commensurability and contrary to the two planets in HD 21693, the innermost planet

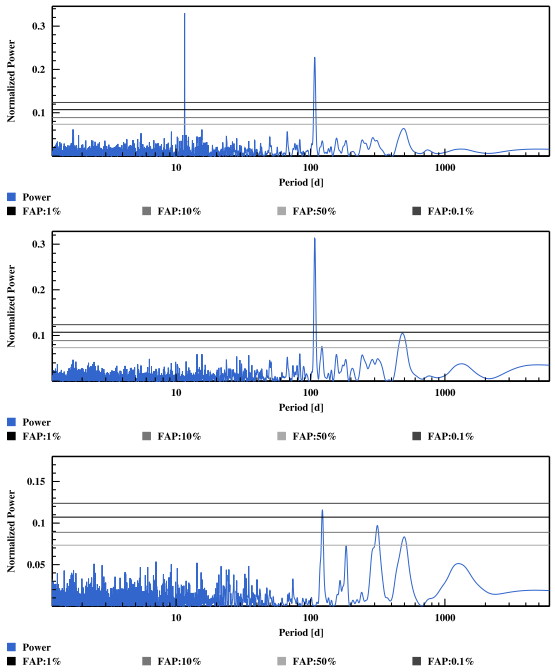

Fig. 22. From top to bottom: GLS periodogram of the residuals at each step, after removing one planet after the other in the analysis of HD 136352. The GLS periodogram of the raw RVs is shown in Fig. 1.

is here on an orbit slightly larger than 5:2 resonance, which is expected for this type of architecture.

6. Conclusion

We have reported the discovery of twenty low-mass planets in eight systems discovered with the HARPS Echelle spectrograph mounted on the 3.6-m ESO telescope located at La Silla Observatory. We also improved the characterization of the extremely eccentric Jupiter orbiting HD20782.

As we can see in Fig. 24, that show in the minimum-mass/period space the planetary detections reported in this paper, we can divide our sample in three mass categories:

- Very small-mass planets with minimum masses below 6 M_{Earth}, that are found orbiting HD 20781 and HD 136352 on short periods, less than 15 days,
- More massive planets in the super-Earth to Neptune transition regime, spanning a range in minimum mass from 8 to 17 M_{Earth}, and a range in period from a few days to nearly a year,
- Massive planet found on long-period orbits.

The RV technique sensitivity goes down when moving towards small-mass and long-period planets. It is therefore not surprising that most of our detection are in the second mass category. The lack of massive object on short-period orbit is already well established, and the detection of extremely small-mass planets, although numerous from *Kepler* statistics (e.g. Coughlin et al. 2015) and previous RV surveys (e.g. Butler et al. 2017; Mayor et al. 2011), is challenging for RV surveys because of stellar signals (Dumusque et al. 2016).

A *Spitzer* dedicated survey looked for transit events induced by the planets orbiting close to their host star, as those would be excellent candidates for further atmospheric characterization as they orbit bright targets (Gillon et al. 2017). Unfortunately, after searching transit events for the innermost planets orbiting HD 20003, HD 20781, HD 31527, HD 45184, HD 51608 and HD 134060, no detection was reported in this study.

Some systems are interesting in terms of architecture. HD20003 host two Neptune-mass planets with periods of 11.9 and 33.9 days, thus close to a 3:1 commensurability. This configuration might explain the relatively high eccentricity measured on the innermost planet in this system. We note also that the two Neptune-mass planets orbiting HD 21693 and the two innermost super-Earth found around HD 136352 are close to a 5:2 resonance. Finally, HD 134060 is also an interesting dynamic system as it harbors a small-mass planet on a 3-day orbit, accompanied by a more massive long-period planet at ~1300 days. The high eccentricity of the inner planet, 0.45, can probably be explained by a Lidov-Kozai mechanism that allowed the migration of the inner planet to a very short-period orbit. Inner planets under the influence of a Lidov-Kozai mechanism should be on inclined orbits relative to the stellar rotational plane (Kozai 1962; Lidov 1961), unfortunately, without any detection of the transit with *Spitzer*, it will be impossible to measure the spin-orbit angle, and therefore to prove this Lidov-Kozai mechanism at play.

The detection of these planets had been announced in Mayor et al. (2011) studying statistical properties of the systems discovered with HARPS. However, with more data in hand, it was possible to discover new *bona-fide* signals. This is the case for the two inner super-Earth orbiting HD20781 and the 13.1-day period super-Earth orbiting HD45184. There is also the 180-day signal found in the timeseries of HD20003, however, as explained in Sec. 5.1, we cannot exclude an instrumental origin to this signal. These new detection shows that gathering more data helps in detecting small-mass planets on short-period orbits as well as long-period signals. Characterising those signals is therefore an expensive, however necessary task.

Acknowledgements. We thank the Swiss National Science Foundation (SNSF) and the Geneva University for their continuous support to our planet search programs. This work has been in particular carried out in the frame of the National Centre for Competence in Research 'PlanetS' supported by the Swiss National Science Foundation (SNSF). XD is grateful to the Society in Science–The Branco Weiss Fellowship for its financial support. N.C.S. was supported by Fundação para a Ciência e a Tecnologia (FCT, Portugal) through the research grant through national funds and by FEDER through COMPETE2020 by grants UID/FIS/04434/2013 & POCI-01-0145-FEDER-007672 and PTDC/FIS-AST/1526/2014 & POCI-01-0145-FEDER-016886, as well as through Investigador FCT contract nr. IF/00169/2012/CP0150/CT0002 funded by FCT and POPH/FSE (EC). PF acknowledges support by Fundação para a Ciência e a Tecnologia (FCT) through Investigador FCT contracts of reference IF/00169/2012/CP0150/CT0002, respectively, and POPH/FSE (EC) by FEDER funding through the program "Programa Operacional de Factores de Competitividade - COMPETE". PF further acknowledges support from Fundação para a Ciência e a Tecnologia (FCT) in the form of an exploratory project of reference IF/01037/2013/CP1191/CT0001. ACC acknowledges support from STFC consolidated grant ST/M001296/1. This research has made use of the SIMBAD database and of the VizieR catalogue access tool operated at CDS, France, and used the DACE platform developed in the frame of PlanetS (`https://dace.unige.ch`).

References

Anderson, D. R., Collier Cameron, A., Hellier, C., et al. 2011, ApJ, 726, L19
Anglada-Escudé, G., López-Morales, M., & Chambers, J. E. 2010, ApJ, 709, 168
Baranne, A., Queloz, D., Mayor, M., et al. 1996, A&AS, 119, 373
Bastien, F. A., Stassun, K. G., Basri, G., & Pepper, J. 2013, Nature, 500, 427
Bastien, F. A., Stassun, K. G., Pepper, J., et al. 2014, AJ, 147, 29
Batalha, N. M., Borucki, W. J., Bryson, S. T., et al. 2011, ApJ, 729, 27
Boisse, I., Bouchy, F., Hébrard, G., et al. 2011, A&A, 528, A4
Borucki, W. J., Koch, D. G., Basri, G., et al. 2011, ApJ, 736, 19
Butler, R. P., Vogt, S. S., Laughlin, G., et al. 2017, AJ, 153, 208
Coughlin, J. L., Mullally, F., Thompson, S. E., et al. 2015, ArXiv e-prints [arXiv:1512.06149]

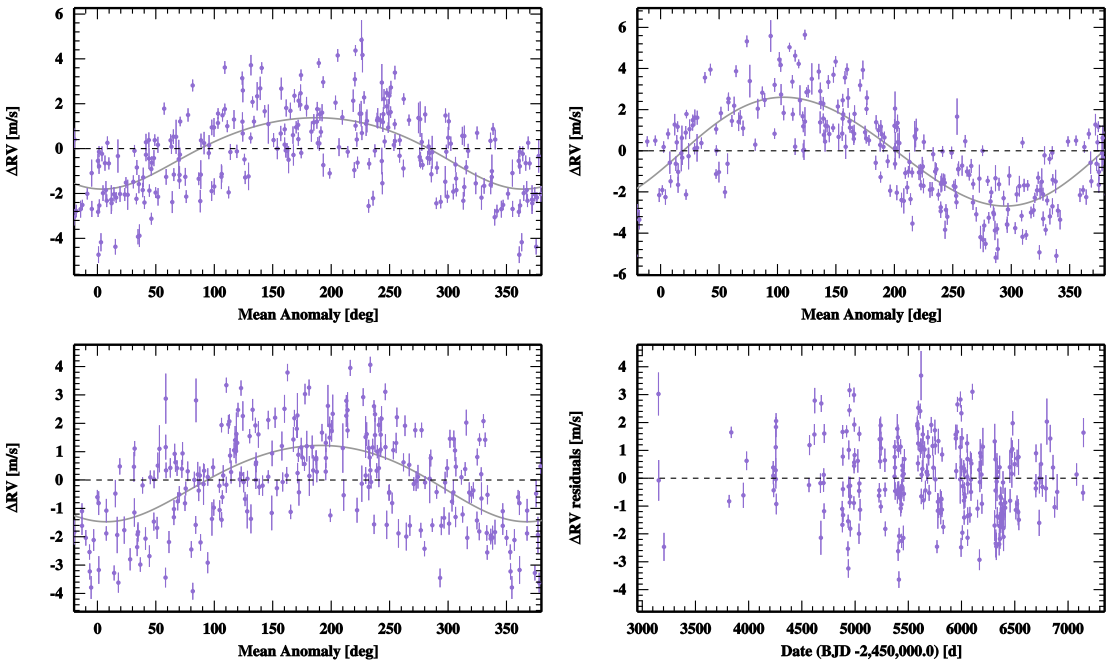

Fig. 23. Phase-folded RV measurements of HD 136352 with, from left to right and top to bottom the best fitted solution for planet b, c and d. The residuals around the solution are displayed in the lower right panel. Corresponding orbital elements are listed in Table 12.

Table 12. Best-fitted solution for the planetary system orbiting HD136352. For each parameter, the median of the posterior is considered, with error bars computed from the MCMC posteriors using a 68.3% confidence interval. The value $\sigma_{(O-C)}$ corresponds to the weighted standard deviation of the residuals around this best solutions. All the parameters probed by the MCMC can be found in Annex, in Table B.9. See Table 4 for definition of the parameters.

Param.	Units	HD136352b	HD136352c	HD136352d
P	[d]	$11.5824^{+0.0024}_{-0.0025}$	$27.5821^{+0.0089}_{-0.0086}$	$107.5983^{+0.2796}_{-0.2669}$
K	[m s^{-1}]	$1.59^{+0.13}_{-0.13}$	$2.65^{+0.14}_{-0.14}$	$1.35^{+0.15}_{-0.15}$
e		$0.14^{+0.08}_{-0.08}$	$0.04^{+0.05}_{-0.03}$	$0.09^{+0.10}_{-0.07}$
ω	[deg]	$-185.64^{+35.97}_{-37.67}$	$-110.22^{+74.58}_{-75.76}$	$170.89^{+63.23}_{-76.56}$
T_P	[d]	$55496.7009^{+1.1393}_{-1.2084}$	$55490.0572^{+5.7741}_{-5.8036}$	$55494.9775^{+18.6996}_{-22.9117}$
T_C	[d]	$55494.3913^{+0.3534}_{-0.3259}$	$55477.8619^{+0.4105}_{-0.3730}$	$55472.4695^{+4.6515}_{-3.2834}$
Ar	[AU]	$0.0934^{+0.0037}_{-0.0040}$	$0.1666^{+0.0066}_{-0.0072}$	$0.4128^{+0.0163}_{-0.0175}$
M.sin i	[M$_{\rm Jup}$]	$0.0151^{+0.0018}_{-0.0018}$	$0.0340^{+0.0034}_{-0.0033}$	$0.0270^{+0.0037}_{-0.0036}$
M.sin i	[M$_{\rm Earth}$]	$4.81^{+0.59}_{-0.56}$	$10.80^{+1.08}_{-1.05}$	$8.58^{+1.18}_{-1.15}$
γ_{HARPS}	[m s^{-1}]		$-68709.0314^{+0.0937}_{-0.0964}$	
$\sigma_{(O-C)}$	[m s^{-1}]		1.35	
log (Post)			$-420.5739^{+2.5027}_{-3.1788}$	

Dawson, R. I. & Fabrycky, D. C. 2010, ApJ, 722, 937
Delisle, J.-B., Ségransan, D., Buchschacher, N., & Alesina, F. 2016, A&A, 590, A134
Desort, M., Lagrange, A.-M., Galland, F., Udry, S., & Mayor, M. 2007, A&A, 473, 983
Díaz, R. F., Almenara, J. M., Santerne, A., et al. 2014, MNRAS, 441, 983
Díaz, R. F., Ségransan, D., Udry, S., et al. 2016, A&A, 585, A134
Díaz, R. F., Ségransan, D., Udry, S., et al. 2015, ArXiv e-prints [arXiv:1510.06446]
Dravins, D. 1982, ARA&A, 20, 61
Dumusque, X., Boisse, I., & Santos, N. C. 2014a, ApJ, 796, 132
Dumusque, X., Bonomo, A. S., Haywood, R. D., et al. 2014b, ApJ, 789, 154
Dumusque, X., Borsa, F., Damasso, M., et al. 2016, submitted to A&A
Dumusque, X., Lovis, C., Ségransan, D., et al. 2011a, A&A, 535, A55
Dumusque, X., Lovis, C., Udry, S., & Santos, N. C. 2011b, in IAU Symposium, Vol. 276, IAU Symposium, ed. A. Sozzetti, M. G. Lattanzi, & A. P. Boss, 530–532
Dumusque, X., Pepe, F., Lovis, C., & Latham, D. W. 2015, ApJ, 808, 171
Dumusque, X., Pepe, F., Lovis, C., et al. 2012, Nature, 491, 207
Dumusque, X., Santos, N. C., Udry, S., Lovis, C., & Bonfils, X. 2011c, A&A, 527, A82
Dumusque, X., Udry, S., Lovis, C., Santos, N. C., & Monteiro, M. J. P. F. G. 2011d, A&A, 525, A140
ESA. 1997, The HIPPARCOS and TYCHO catalogue, ESA-SP 1200
Fabrycky, D. C., Lissauer, J. J., Ragozzine, D., et al. 2014, ApJ, 790, 146
Gillon, M., Demory, B.-O., Lovis, C., et al. 2017, ArXiv e-prints [arXiv:1701.01303]
Gomes da Silva, J., Santos, N. C., Bonfils, X., et al. 2011, A&A, 534, A30

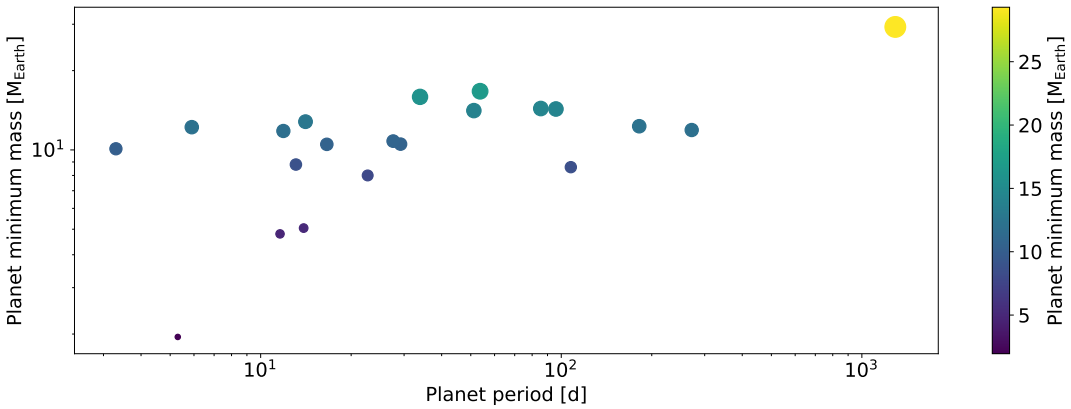

Fig. 24. Summary of the detected planetary signals in the minimum mass - period space.

Gray, R. O., Corbally, C. J., Garrison, R. F., et al. 2006, AJ, 132, 161
Haywood, R. D., Collier Cameron, A., Queloz, D., et al. 2014, MNRAS, 443, 2517
Haywood, R. D., Collier Cameron, A., Unruh, Y. C., et al. 2016, MNRAS, 457, 3637
Jones, H. R. A., Butler, R. P., Tinney, C. G., et al. 2006, MNRAS, 369, 249
Kozai, Y. 1962, AJ, 67, 591
Latham, D. W., Rowe, J. F., Quinn, S. N., et al. 2011, ApJ, 732, L24
Lidov, M. L. 1961, Planetary and Space Science, 9, 719
Lissauer, J. J., Fabrycky, D. C., Ford, E. B., et al. 2011, Nature, 470, 53
Lissauer, J. J., Marcy, G. W., Bryson, S. T., et al. 2014, ApJ, 784, 44
Lo Curto, G., Mayor, M., Benz, W., et al. 2013, A&A, 551, A59
Lovis, C., Dumusque, X., Santos, N. C., et al. 2011a, ArXiv e-prints [arXiv:1107.5325]
Lovis, C., Mayor, M., Bouchy, F., et al. 2009, in IAU Symposium, Vol. 253, IAU Symposium, 502–505
Lovis, C., Mayor, M., Pepe, F., et al. 2006, Nature, 441, 305
Lovis, C., Mayor, M., Pepe, F., Queloz, D., & Udry, S. 2008, in Precision Spectroscopy in Astrophysics, ed. N. C. Santos, L. Pasquini, A. C. M. Correia, & M. Romaniello, 181–184
Lovis, C., Ségransan, D., Mayor, M., et al. 2011b, A&A, 528, A112+
Mamajek, E. E. & Hillenbrand, L. A. 2008, ApJ, 687, 1264
Mayor, M., Marmier, M., Lovis, C., et al. 2011, ArXiv e-prints [arXiv:1109.2497]
Mayor, M., Pepe, F., Queloz, D., et al. 2003, The Messenger, 114, 20
Mayor, M., Udry, S., Lovis, C., et al. 2009, A&A, 493, 639
Meunier, N., Desort, M., & Lagrange, A.-M. 2010, A&A, 512, A39
Meunier, N. & Lagrange, A.-M. 2013, A&A, 551, A101
Meunier, N., Lagrange, A.-M., Mbemba Kabuiku, L., et al. 2016, ArXiv e-prints [arXiv:1610.02168]
Motalebi, F., Udry, S., Gillon, M., et al. 2015, A&A, 584, A72
Moutou, C., Lo Curto, G., Mayor, M., et al. 2015, A&A, 576, A48
Moutou, C., Mayor, M., Lo Curto, G., et al. 2011, A&A, 527, A63+
Mowlavi, N., Eggenberger, P., Meynet, G., et al. 2012, A&A, 541, A41
Mullally, F., Coughlin, J. L., Thompson, S. E., et al. 2015, ApJS, 217, 31
Noyes, R., Hartmann, L., Baliunas, S., Duncan, D., & Vaughan, A. 1984, ApJ, 279, 763
Pepe, F., Lovis, C., Ségransan, D., et al. 2011, A&A, 534, A58
Pepe, F., Mayor, M., Delabre, B., et al. 2000, in Optical and IR Telescope Instrumentation and Detectors, Proc. SPIE Vol. 4008, ed. A. Moorwood, Vol. 4008, 582–592
Pepe, F., Mayor, M., Galland, F., et al. 2002, A&A, 388, 632
Queloz, D., Bouchy, F., Moutou, C., et al. 2009, A&A, 506, 303
Queloz, D., Eggenberger, A., Mayor, M., et al. 2000, A&A, 359, L13
Rogers, L. A. 2015, ApJ, 801, 41
Saar, S. & Donahue, R. 1997, ApJ, 485, 319
Santos, N., Mayor, M., Naef, D., et al. 2000, A&A, 361, 265
Santos, N., Mayor, M., Naef, D., et al. 2002, A&A, 392, 215
Scargle, J. D. 1982, ApJ, 263, 835
Selsis, F., Kasting, J. F., Levrard, B., et al. 2007, A&A, 476, 1373
Sousa, S. G., Santos, N. C., Mayor, M., et al. 2008, A&A, 487, 373
Udry, S., Mayor, M., Naef, D., et al. 2000, A&A, 356, 590
Udry, S. & Santos, N. C. 2007, ARA&A, 45, 397
van Leeuwen, F. 2007, A&A, 474, 653
Vaughan, A., Preston, G., & Wilson, O. 1978, PASP, 90, 267
Vogt, S. S., Wittenmyer, R. A., Butler, R. P., et al. 2010, ApJ, 708, 1366
Weiss, L. M. & Marcy, G. W. 2014, ApJ, 783, L6
Wilken, T., Lovis, C., Manescau, A., et al. 2010, Monthly Notices of the Royal Astronomical Society: Letters, 405, L16
Wilson, O. C. 1968, ApJ, 153, 221
Wolfgang, A. & Lopez, E. 2015, ApJ, 806, 183
Zechmeister, M. & Kürster, M. 2009, A&A, 496, 577

Appendix A: Periodogram of the activity and CCF indicators

To check if any signal detected in RVs corresponds to signals measured in activity indicator, we show here the periodograms of the $\log(R'_{HK})$,the BIS SPAN and the FWHM. Those indicators have been shown to be sensitive to activity, and therefore any signal appearing both in the RVs and at least one of those indicators might be induced by stellar activity. Because magnetic cycles will be seen as a long-period significant signals in all those indicators, we removed any long-term signal either by fitting a Keplerian to adjust at best the observed magnetic cycle, as in Fig. 1, or by adjusting a second order polynomial.

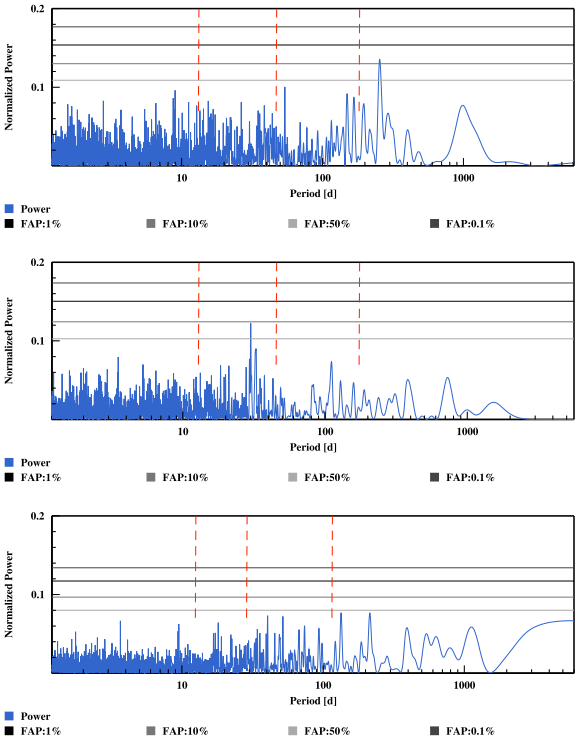

Fig. A.1. From top to bottom, periodograms of the $\log(R'_{HK})$, BIS SPAN and FWHM residuals of HD20003 after fitting either a Keplerian to adjust at best the observed magnetic cycles or a second order polynomial to take into account any drift that could be instrumental. Planetary signals announced in Sec. 5 are represented by dashed vertical red lines.

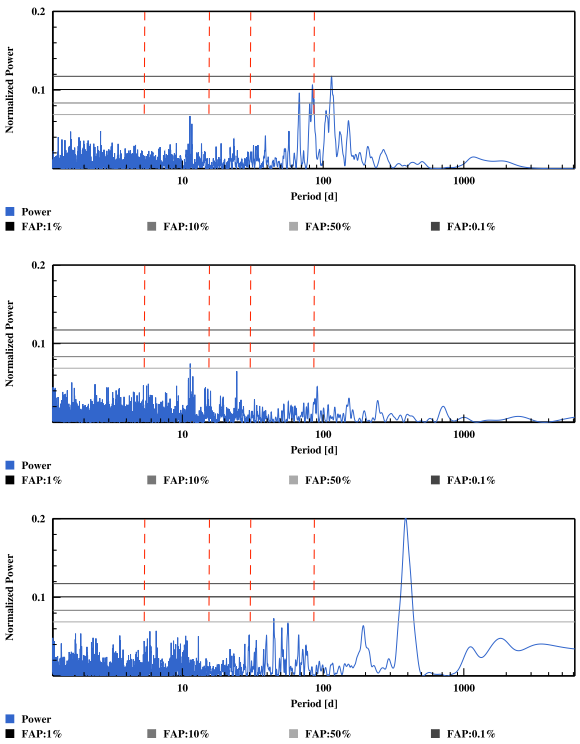

Fig. A.2. Same as Fig. A.1 but for HD20781

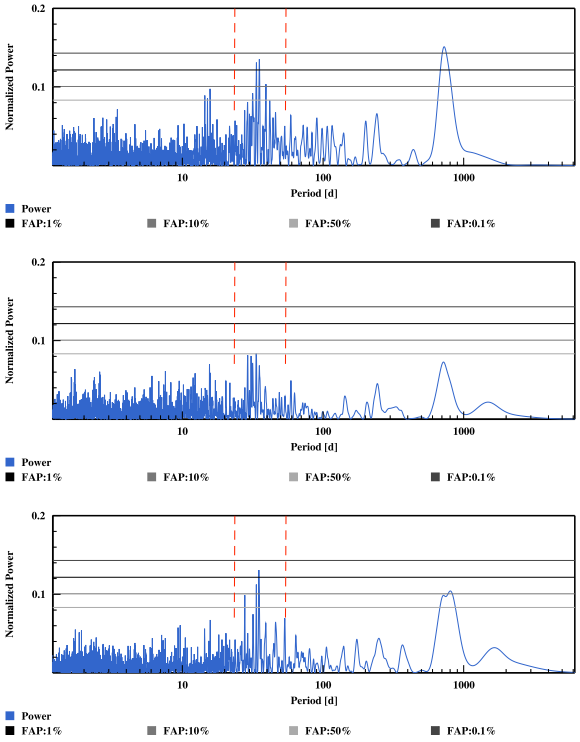

Fig. A.3. Same as Fig. A.1 but for HD21693

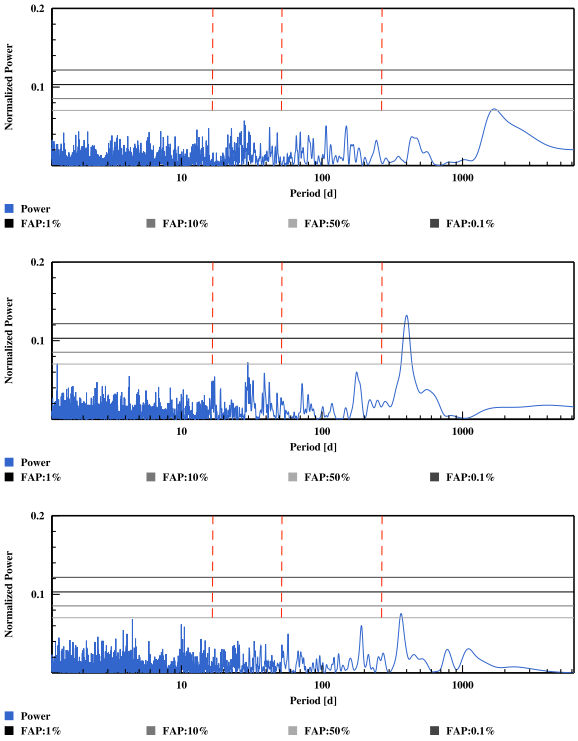

Fig. A.4. Same as Fig. A.1 but for HD31527

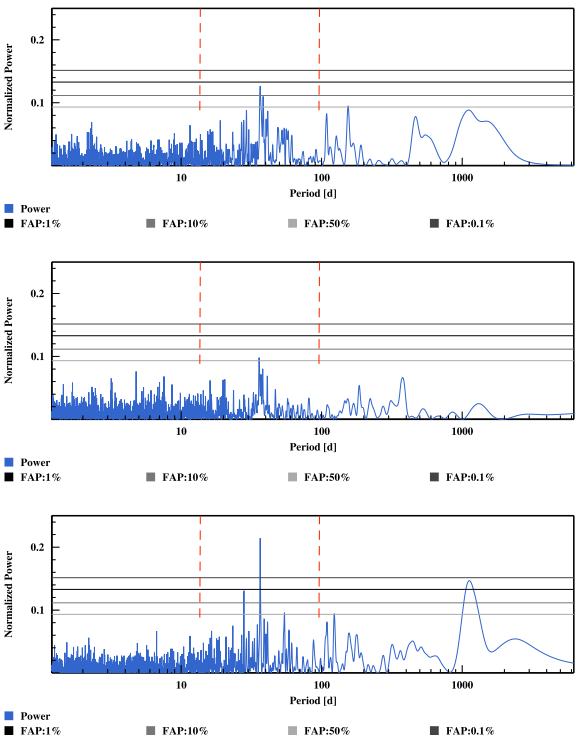

Fig. A.6. Same as Fig. A.1 but for HD51608

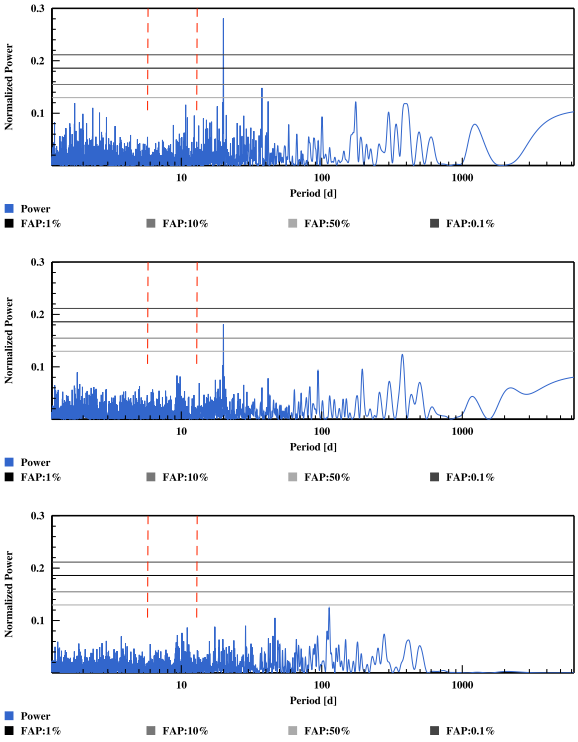

Fig. A.5. Same as Fig. A.1 but for HD45184

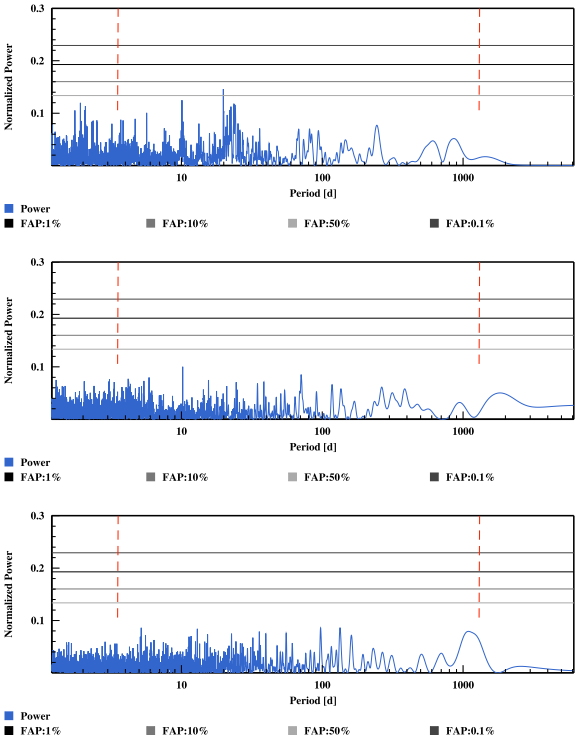

Fig. A.7. Same as Fig. A.1 but for HD134060

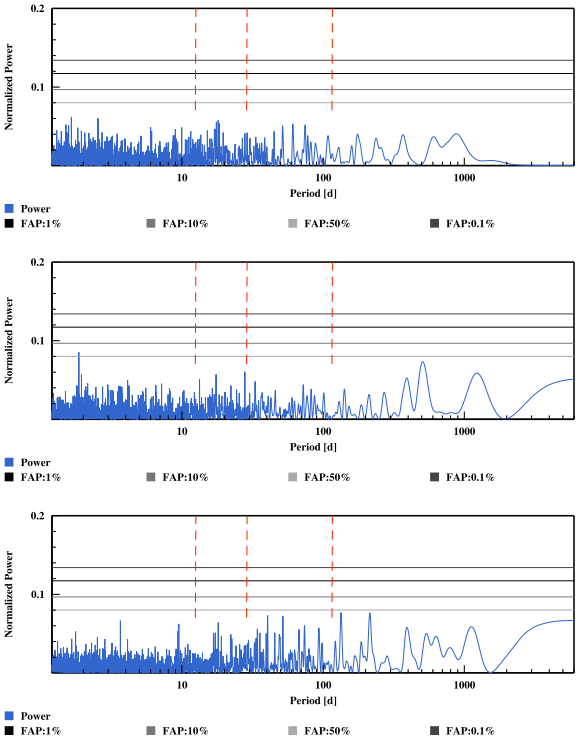

Fig. A.8. Same as Fig. A.1 but for HD136352

Appendix B: Parameters probed by MCMC

We present in this appendix all the parameters probed by our MCMC when fitting each planetary system.

Table B.1. Parameters probed by the MCMC used to fit the RV measurements of HD20003. The maximum likelihood solution (Max(Like)), the median (Med), mode (Mod) and standard deviation (Std) of the posterior distribution for each parameter is shown, as well as the 68.3% (CI(15.85),CI(84.15)) and 95.45% (CI(2.275),CI(97.725)) confidence intervals. The prior for each parameter can be of type: $\mathcal{U}$: uniform, $\mathcal{N}$: normal, or Fixed if values were not fitted.

Param.	Units	Max(Like)	Med	Mod	Std	CI(15.85)	CI(84.15)	CI(2.275)	CI(97.725)	Prior
					Likelihood					
log (Post)		-355.828813	-363.907150	-364.131854	2.832208	-367.455747	-361.063533	-371.658400	-358.829760	
log (Like)		-354.602155	-362.792512	-362.951597	2.835282	-366.320092	-359.929955	-370.559936	-357.677435	
log (Prior)		-1.226658	-1.103442	-1.117157	0.241152	-1.394048	-0.862677	-1.788151	-0.652519	
$M_\star$	[$M_\odot$]	0.816085	0.874814	0.879368	0.088444	0.775774	0.975894	0.675624	1.081234	$\mathcal{N}(0.875, 0.1)$
σ_{HARPS}	[m s^{-1}]	1.43	1.50	1.49	0.09	1.40	1.61	1.30	1.74	$\mathcal{U}$
γ_{HARPS}	[m s^{-1}]	-16103.93	-16103.88	-16103.95	0.37	-16104.31	-16103.48	-16104.75	-16103.07	$\mathcal{U}$
lin	[m s^{-1} yr^{-1}]	-0.96	-1.00	-1.02	0.06	-1.07	-0.94	-1.14	-0.86	$\mathcal{U}$
quad	[m s^{-1} yr^{-2}]	-0.18	-0.18	-0.20	0.04	-0.23	-0.13	-0.27	-0.08	$\mathcal{U}$
log (P)	[d]	1.073690	1.073702	1.073700	0.000048	1.073647	1.073757	1.073596	1.073809	$\mathcal{U}$
log (K)	[m s^{-1}]	0.60	0.58	0.57	0.02	0.56	0.60	0.53	0.63	$\mathcal{U}$
$\sqrt{e}.\cos\omega$		-0.038788	-0.030935	-0.031087	0.078054	-0.117912	0.059001	-0.208228	0.146078	$\mathcal{U}$
$\sqrt{e}.\sin\omega$		-0.637556	-0.609524	-0.623678	0.036763	-0.648609	-0.565355	-0.686138	-0.514327	$\mathcal{U}$
λ_0	[deg]	-134.804759	-134.245134	-134.267579	3.068764	-137.793675	-130.856228	-141.494828	-127.394865	$\mathcal{U}$
log (P)	[d]	1.530129	1.530192	1.530160	0.000253	1.529916	1.530498	1.529687	1.530787	$\mathcal{U}$
log (K)	[m s^{-1}]	0.51	0.50	0.51	0.02	0.48	0.53	0.45	0.55	$\mathcal{U}$
$\sqrt{e}.\cos\omega$		0.042914	0.080507	0.079367	0.147537	-0.106427	0.244455	-0.241255	0.364645	$\mathcal{U}$
$\sqrt{e}.\sin\omega$		0.230156	0.160674	0.214983	0.135058	-0.019597	0.294386	-0.171598	0.388346	$\mathcal{U}$
λ_0	[deg]	127.212419	124.039354	123.641257	3.267942	120.338440	127.741186	116.668939	131.353482	$\mathcal{U}$
log (P)	[d]	2.264075	2.263903	2.263414	0.002162	2.261436	2.266346	2.258832	2.268814	$\mathcal{U}$
log (K)	[m s^{-1}]	0.16	0.20	0.19	0.05	0.14	0.25	0.07	0.30	$\mathcal{U}$
$\sqrt{e}.\cos\omega$		0.163835	0.145216	0.267150	0.204587	-0.116791	0.366532	-0.331884	0.514769	$\mathcal{U}$
$\sqrt{e}.\sin\omega$		0.388909	0.201337	0.286104	0.195568	-0.058872	0.396069	-0.281096	0.531697	$\mathcal{U}$
λ_0	[deg]	200.534506	200.366201	199.500808	6.212750	193.253677	207.254185	185.477481	214.320934	$\mathcal{U}$
log (P)	[d]	3.518224	3.518224	3.518224	0.000000	3.518224	3.518224	3.518224	3.518224	Fixed
log (K)	[m s^{-1}]	0.72	0.71	0.70	0.04	0.67	0.75	0.61	0.78	$\mathcal{U}$
$\sqrt{e}.\cos\omega$		0.206349	0.206349	0.206349	0.000000	0.206349	0.206349	0.206349	0.206349	Fixed
$\sqrt{e}.\sin\omega$		-0.312282	-0.312282	-0.312282	0.000000	-0.312282	-0.312282	-0.312282	-0.312282	Fixed
λ_0	[deg]	-191.112000	-191.112000	-191.112000	0.000000	-191.112000	-191.112000	-191.112000	-191.112000	Fixed

Table B.2. Parameters probed by the MCMC used to fit the RV measurements of HD20781. The maximum likelihood solution (Max(Like)), the median (Med), mode (Mod) and standard deviation (Std) of the posterior distribution for each parameter is shown, as well as the 68.3% (CI(15.85),CI(84.15)) and 95.45% (CI(2.275),CI(97.725)) confidence intervals. The prior for each parameter can be of type: $\mathcal{U}$: uniform, $\mathcal{N}$: normal.

Param.	Units	Max(Like)	Med	Mod	Std	CI(15.85)	CI(84.15)	CI(2.275)	CI(97.725)	Prior
					Likelihood					
log (Post)		-388.542397	-397.139540	-396.801832	3.086207	-400.992042	-394.045214	-405.822507	-391.632479	
log (Like)		-388.379068	-396.816561	-396.641259	3.045776	-400.618909	-393.744957	-405.246050	-391.364866	
log (Prior)		-0.163328	-0.271536	-0.192668	0.188786	-0.532565	-0.133491	-0.959781	-0.053132	
$M_\star$	[$M_\odot$]	0.798309	0.700500	0.675260	0.088466	0.599877	0.801716	0.500287	0.905060	$\mathcal{N}(0.7, 0.1)$
σ_{JIT}	[m s^{-1}]	1.14	1.27	1.21	0.19	1.09	1.01	1.00	0.69	$\mathcal{U}$
γ_{HARPS}	[m s^{-1}]	40369.22	40369.21	40369.17	0.10	40369.10	40369.32	40368.98	40369.44	$\mathcal{U}$
log (P)	[d]	0.725379	0.725377	0.725315	0.000076	0.725292	0.725459	0.725196	0.725567	$\mathcal{U}$
log (K)	[m s^{-1}]	0.05	-0.04	-0.04	0.07	-0.12	0.03	-0.22	0.09	$\mathcal{U}$
$\sqrt{e}.\cos\omega$		-0.061140	0.043862	0.039181	0.230069	-0.243492	0.299379	-0.460848	0.499573	$\mathcal{U}$
$\sqrt{e}.\sin\omega$		0.216991	-0.013862	-0.028798	0.215428	-0.264618	0.241274	-0.455895	0.436077	$\mathcal{U}$
λ_0	[deg]	-135.345360	-134.251473	-137.352873	9.387901	-144.854378	-123.506806	-156.133446	-112.221519	$\mathcal{U}$
log (P)	[d]	1.142791	1.142717	1.142690	0.000092	1.142611	1.142819	1.142490	1.142923	$\mathcal{U}$
log (K)	[m s^{-1}]	0.29	0.26	0.24	0.03	0.22	0.29	0.18	0.33	$\mathcal{U}$
$\sqrt{e}.\cos\omega$		0.327288	0.203741	0.321124	0.172122	-0.029464	0.370760	-0.219811	0.484086	$\mathcal{U}$
$\sqrt{e}.\sin\omega$		0.021983	0.026817	0.016131	0.159055	-0.169199	0.211170	-0.318653	0.343092	$\mathcal{U}$
λ_0	[deg]	-84.722610	-83.737346	-84.982562	4.380473	-88.530458	-78.631060	-93.607328	-73.479892	$\mathcal{U}$
log (P)	[d]	1.464692	1.464758	1.464755	0.000134	1.464609	1.464910	1.464452	1.465071	$\mathcal{U}$
log (K)	[m s^{-1}]	0.45	0.45	0.45	0.02	0.42	0.48	0.40	0.50	$\mathcal{U}$
$\sqrt{e}.\cos\omega$		0.139677	0.145327	0.162099	0.120006	-0.010957	0.265346	-0.162692	0.358965	$\mathcal{U}$
$\sqrt{e}.\sin\omega$		0.246274	0.263747	0.306374	0.113409	0.114332	0.358597	-0.077325	0.434823	$\mathcal{U}$
λ_0	[deg]	-77.213730	-78.248282	-78.600903	2.996830	-81.624509	-74.896708	-84.983023	-71.294902	$\mathcal{U}$
log (P)	[d]	1.931848	1.932003	1.932093	0.000430	1.931522	1.932502	1.931041	1.932995	$\mathcal{U}$
log (K)	[m s^{-1}]	0.43	0.41	0.41	0.02	0.39	0.44	0.37	0.46	$\mathcal{U}$
$\sqrt{e}.\cos\omega$		0.148239	0.050362	0.090292	0.146393	-0.126620	0.219662	-0.260249	0.340229	$\mathcal{U}$
$\sqrt{e}.\sin\omega$		0.268142	0.155008	0.226421	0.139655	-0.035773	0.293236	-0.188818	0.387469	$\mathcal{U}$
λ_0	[deg]	12.584852	15.024637	14.339843	3.408448	11.079349	18.883891	7.424984	22.814245	$\mathcal{U}$

Table B.3. Parameters probed by the MCMC used to fit the RV measurements of HD20782. The maximum likelihood solution (Max(Like)), the median (Med), mode (Mod) and standard deviation (Std) of the posterior distribution for each parameter is shown, as well as the 68.3% (CI(15.85),CI(84.15)) and 95.45% (CI(2.275),CI(97.725)) confidence intervals. The prior for each parameter can be of type: $\mathcal{U}$: uniform, $\mathcal{N}$: normal.

Param.	Units	Max(Like)	Med	Mod	Std	CI(15.85)	CI(84.15)	CI(2.275)	CI(97.725)	Prior
					Likelihood					
log (Post)		-372.933997	-379.659609	-379.184909	2.652630	-382.940155	-377.007478	-387.071255	-375.024009	
log (Like)		-367.930148	-374.651836	-374.180899	2.652279	-377.934595	-371.997235	-382.071125	-370.018358	
log (Prior)		-5.003849	-5.008809	-5.011567	0.009534	-5.019713	-4.997733	-5.030582	-4.987338	
$M_\star$	[$M_\odot$]	0.985227	0.950073	0.916830	0.087670	0.850317	1.050787	0.755244	1.148009	$\mathcal{N}(0.95, 0.1)$
$\sigma_{COR07-DRS-3-4}$	[m s^{-1}]	5.33	6.45	5.20	1.77	4.84	8.72	3.61	12.03	$\mathcal{U}$
$\sigma_{COR14-DRS-3-8}$	[m s^{-1}]	4.32	4.66	4.01	1.59	3.08	6.58	1.49	9.29	$\mathcal{U}$
$\sigma_{COR98-DRS-3-3}$	[m s^{-1}]	5.26	5.88	5.33	1.74	4.14	7.98	2.33	10.72	$\mathcal{U}$
σ_{HARPS}	[m s^{-1}]	1.42	1.49	1.47	0.21	1.25	1.71	1.00	1.95	$\mathcal{U}$
$\sigma_{UCLES-PUB-2006}$	[m s^{-1}]	0.06	1.60	0.00	1.05	0.49	2.95	0.07	4.41	$\mathcal{U}$
σ_{JIT}	[m s^{-1}]	1.29	0.94	1.00	0.46	0.37	1.47	0.06	1.93	$\mathcal{U}$
$\gamma_{COR07-DRS-3-4}$	[m s^{-1}]	39931.00	39930.61	39930.34	1.92	39928.44	39932.70	39925.88	39935.32	$\mathcal{U}$
$\gamma_{COR14-DRS-3-8}$	[m s^{-1}]	39958.04	39956.56	39956.34	1.46	39954.89	39958.14	39952.82	39959.96	$\mathcal{U}$
$\gamma_{COR98-DRS-3-3}$	[m s^{-1}]	39929.00	39928.10	39927.80	1.68	39926.19	39929.98	39924.15	39932.04	$\mathcal{U}$
γ_{HARPS}	[m s^{-1}]	39964.88	39964.81	39964.82	0.20	39964.58	39965.03	39964.35	39965.25	$\mathcal{U}$
offset$_{UCLES-PUB-2006}$	[m s^{-1}]	5.30	5.44	5.26	0.83	4.51	6.37	3.53	7.36	$\mathcal{U}$
log (P)	[d]	2.776014	2.776021	2.776014	0.000016	2.776003	2.776040	2.775987	2.776056	$\mathcal{U}$
log (K)	[m s^{-1}]	2.07	2.07	2.07	0.01	2.07	2.08	2.06	2.09	$\mathcal{U}$
$\sqrt{e}.\cos\omega$		-0.780714	-0.784083	-0.787192	0.005216	-0.789895	-0.777061	-0.793328	-0.773612	$\mathcal{U}$
$\sqrt{e}.\sin\omega$		0.582695	0.578516	0.573850	0.006592	0.571141	0.587284	0.566660	0.591712	$\mathcal{U}$
λ_0	[deg]	295.804494	296.111799	296.327571	0.488659	295.460223	296.661315	295.142950	296.986011	$\mathcal{U}$

Table B.4. Parameters probed by the MCMC used to fit the RV measurements of HD21693. The maximum likelihood solution (Max(Like)), the median (Med), mode (Mod) and standard deviation (Std) of the posterior distribution for each parameter is shown, as well as the 68.3% (CI(15.85),CI(84.15)) and 95.45% (CI(2.275),CI(97.725)) confidence intervals. The prior for each parameter can be of type: $\mathcal{U}$: uniform, $\mathcal{N}$: normal.

Param.	Units	Max(Like)	Med	Mod	Std	CI(15.85)	CI(84.15)	CI(2.275)	CI(97.725)	Prior
					Likelihood					
log (Post)		-435.045817	-440.915985	-440.662807	2.436011	-444.034771	-438.620178	-447.941122	-436.845354	
log (Like)		-434.994431	-440.747390	-440.523392	2.426114	-443.837350	-438.463925	-447.707065	-436.680607	
log (Prior)		-0.051386	-0.133026	-0.077867	0.126005	-0.308420	-0.041395	-0.592687	-0.007046	
$M_\star$	[$M_\odot$]	0.627847	0.799037	0.801958	0.087416	0.699111	0.898724	0.600636	0.995794	$\mathcal{N}(0.8, 0.1)$
$\sigma_{JIT\ LOW}$	[m s^{-1}]	1.27	1.26	1.25	0.44	0.73	0.79	0.14	0.38	$\mathcal{U}$
$\sigma_{JIT\ HIGH}$	[m s^{-1}]	2.69	2.56	2.70	0.56	1.86	2.06	0.85	1.60	$\mathcal{U}$
γ_{HARPS}	[m s^{-1}]	39768.81	39768.81	39768.82	0.13	39768.66	39768.95	39768.52	39769.09	$\mathcal{U}$
RHK$_{index}$ *lin*	[m s^{-1} RHD$_{index}^{-1}$]	11.066005	10.860734	10.732702	0.440301	10.361899	11.369837	9.877045	11.871009	$\mathcal{U}$
log (P)	[d]	1.355767	1.355617	1.355612	0.000146	1.355449	1.355780	1.355285	1.355943	$\mathcal{U}$
log (K)	[m s^{-1}]	0.35	0.34	0.34	0.04	0.30	0.38	0.24	0.42	$\mathcal{U}$
$\sqrt{e}.\cos\omega$		-0.033137	-0.003440	-0.067300	0.179167	-0.215702	0.205008	-0.392233	0.358369	$\mathcal{U}$
$\sqrt{e}.\sin\omega$		-0.247432	-0.267481	-0.370194	0.162410	-0.411532	-0.042976	-0.522567	0.169768	$\mathcal{U}$
λ_0	[deg]	34.107432	35.450889	33.905458	4.533112	30.349272	40.588204	25.065784	46.053381	$\mathcal{U}$
log (P)	[d]	1.730230	1.730263	1.730205	0.000221	1.730013	1.730515	1.729784	1.730800	$\mathcal{U}$
log (K)	[m s^{-1}]	0.54	0.54	0.54	0.02	0.51	0.56	0.48	0.59	$\mathcal{U}$
$\sqrt{e}.\cos\omega$		0.269425	0.196029	0.243736	0.136666	0.005735	0.324520	-0.157091	0.416385	$\mathcal{U}$
$\sqrt{e}.\sin\omega$		-0.025692	-0.063953	-0.075276	0.137633	-0.218240	0.105252	-0.335603	0.237976	$\mathcal{U}$
λ_0	[deg]	-206.679521	-207.980760	-207.807573	2.957609	-211.285700	-204.615563	-214.868823	-201.248502	$\mathcal{U}$

Table B.5. Parameters probed by the MCMC used to fit the RV measurements of HD31527. The maximum likelihood solution (Max(Like)), the median (Med), mode (Mod) and standard deviation (Std) of the posterior distribution for each parameter is shown, as well as the 68.3% (CI(15.85),CI(84.15)) and 95.45% (CI(2.275),CI(97.725)) confidence intervals. The prior for each parameter can be of type: $\mathcal{U}$: uniform, $\mathcal{N}$: normal.

Param.	Units	Max(Like)	Med	Mod	Std	CI(15.85)	CI(84.15)	CI(2.275)	CI(97.725)	Prior
					Likelihood					
log (Post)		-431.457393	-439.413776	-439.404479	2.693424	-442.806691	-436.678805	-446.790781	-434.536716	
log (Like)		-430.869912	-438.920421	-438.066741	2.744421	-442.319982	-436.104557	-446.392727	-433.960853	
log (Prior)		-0.587481	-0.421477	-0.228174	0.322560	-0.872877	-0.155258	-1.460968	-0.044428	
$M_\star$	[$M_\odot$]	0.964548	0.960466	0.935623	0.087688	0.861241	1.058519	0.761776	1.159099	$\mathcal{N}(0.96, 0.1)$
σ_{JIT}	[m s^{-1}]	1.24	1.29	1.29	0.30	0.95	0.93	0.77	0.62	$\mathcal{U}$
γ_{HARPS}	[m s^{-1}]	25739.68	25739.70	25739.69	0.09	25739.61	25739.80	25739.51	25739.90	$\mathcal{U}$
log (P)	[d]	1.218857	1.218889	1.218885	0.000080	1.218798	1.218979	1.218706	1.219071	$\mathcal{U}$
log (K)	[m s^{-1}]	0.43	0.43	0.43	0.02	0.41	0.46	0.39	0.48	$\mathcal{U}$
$\sqrt{e}.\cos\omega$		0.242808	0.210416	0.235029	0.104713	0.075031	0.311766	-0.082660	0.383529	$\mathcal{U}$
$\sqrt{e}.\sin\omega$		0.236848	0.188237	0.211870	0.120112	0.021413	0.298912	-0.126407	0.384773	$\mathcal{U}$
λ_0	[deg]	52.547369	51.262624	51.323989	2.622456	48.258036	54.220352	45.382590	57.230513	$\mathcal{U}$
log (P)	[d]	1.709426	1.709315	1.709215	0.000282	1.709003	1.709631	1.708664	1.709963	$\mathcal{U}$
log (K)	[m s^{-1}]	0.40	0.40	0.40	0.02	0.37	0.42	0.35	0.45	$\mathcal{U}$
$\sqrt{e}.\cos\omega$		0.023117	0.081468	0.086880	0.144497	-0.097212	0.242734	-0.237589	0.358056	$\mathcal{U}$
$\sqrt{e}.\sin\omega$		-0.164323	0.014834	-0.010018	0.126248	-0.134951	0.164944	-0.248677	0.274415	$\mathcal{U}$
λ_0	[deg]	-208.406874	-207.583870	-207.914089	2.785788	-210.745542	-204.465797	-213.962526	-201.198653	$\mathcal{U}$
log (P)	[d]	2.434889	2.434048	2.433252	0.003107	2.430440	2.437413	2.426290	2.440704	$\mathcal{U}$
log (K)	[m s^{-1}]	0.11	0.10	0.09	0.05	0.04	0.15	-0.03	0.21	$\mathcal{U}$
$\sqrt{e}.\cos\omega$		-0.541593	-0.450052	-0.536450	0.169210	-0.588081	-0.235463	-0.692747	0.104560	$\mathcal{U}$
$\sqrt{e}.\sin\omega$		0.097884	0.006756	0.058079	0.173485	-0.200976	0.195484	-0.403356	0.363079	$\mathcal{U}$
λ_0	[deg]	-111.177767	-110.997045	-113.124819	5.834754	-117.548307	-104.311167	-124.016867	-97.254697	$\mathcal{U}$

Table B.6. Parameters probed by the MCMC used to fit the RV measurements of HD45184. The maximum likelihood solution (Max(Like)), the median (Med), mode (Mod) and standard deviation (Std) of the posterior distribution for each parameter is shown, as well as the 68.3% (CI(15.85),CI(84.15)) and 95.45% (CI(2.275),CI(97.725)) confidence intervals. The prior for each parameter can be of type: $\mathcal{U}$: uniform, $\mathcal{N}$: normal.

Param.	Units	Max(Like)	Med	Mod	Std	CI(15.85)	CI(84.15)	CI(2.275)	CI(97.725)	Prior
					Likelihood					
log (Post)		-375.948188	-382.533843	-381.953342	2.376383	-385.497577	-380.151077	-389.208051	-378.372729	
log (Like)		-375.907261	-382.434308	-381.860465	2.358405	-385.390539	-380.066476	-389.064124	-378.293195	
log (Prior)		-0.040927	-0.076679	-0.029834	0.074946	-0.179107	-0.022112	-0.352708	-0.003342	
$M_\star$	[$M_\odot$]	1.058757	1.029104	1.010914	0.087356	0.930545	1.127460	0.830397	1.231321	$\mathcal{N}(1.03, 0.1)$
$\sigma_{JIT\ LOW}$	[m s^{-1}]	1.38	1.76	1.90	0.64	0.73	1.27	0.11	0.83	$\mathcal{U}$
$\sigma_{JIT\ HIGH}$	[m s^{-1}]	2.33	2.74	2.77	0.68	1.70	2.17	0.93	1.62	$\mathcal{U}$
γ_{HARPS}	[m s^{-1}]	-3757.68	-3757.65	-3757.69	0.14	-3757.81	-3757.49	-3757.98	-3757.34	$\mathcal{U}$
RHK_{index} *lin*	[m s^{-1} $RHD_{index}{}^{-1}$]	10.723380	10.634926	10.630724	0.607624	9.941268	11.330657	9.258677	11.996205	$\mathcal{U}$
log (P)	[d]	0.769779	0.769779	0.769776	0.000020	0.769758	0.769802	0.769736	0.769826	$\mathcal{U}$
log (K)	[m s^{-1}]	0.63	0.63	0.63	0.02	0.61	0.65	0.58	0.67	$\mathcal{U}$
$\sqrt{e}.\cos\omega$		-0.220553	-0.170838	-0.275286	0.126595	-0.294336	-0.000876	-0.378620	0.156389	$\mathcal{U}$
$\sqrt{e}.\sin\omega$		0.182613	0.117241	0.149405	0.131397	-0.053453	0.252324	-0.200167	0.349677	$\mathcal{U}$
λ_0	[deg]	-230.080798	-229.352706	-229.816814	2.694368	-232.391963	-226.300698	-235.479746	-223.032360	$\mathcal{U}$
log (P)	[d]	1.118470	1.118443	1.118431	0.000075	1.118359	1.118527	1.118271	1.118619	$\mathcal{U}$
log (K)	[m s^{-1}]	0.40	0.37	0.37	0.04	0.33	0.41	0.28	0.45	$\mathcal{U}$
$\sqrt{e}.\cos\omega$		-0.147627	-0.073911	-0.085546	0.176247	-0.277303	0.140983	-0.420074	0.304579	$\mathcal{U}$
$\sqrt{e}.\sin\omega$		-0.059901	0.065831	0.087988	0.173593	-0.146692	0.260735	-0.312367	0.404779	$\mathcal{U}$
λ_0	[deg]	-129.227327	-127.324650	-126.147264	4.833219	-132.789170	-121.833139	-138.259570	-116.150675	$\mathcal{U}$

Table B.7. Parameters probed by the MCMC used to fit the RV measurements of HD51608. The maximum likelihood solution (Max(Like)), the median (Med), mode (Mod) and standard deviation (Std) of the posterior distribution for each parameter is shown, as well as the 68.3% (CI(15.85),CI(84.15)) and 95.45% (CI(2.275),CI(97.725)) confidence intervals. The prior for each parameter can be of type: $\mathcal{U}$: uniform, $\mathcal{N}$: normal.

Param.	Units	Max(Like)	Med	Mod	Std	CI(15.85)	CI(84.15)	CI(2.275)	CI(97.725)	Prior
					Likelihood					
log (Post)		-402.833168	-409.139845	-408.668989	2.465262	-412.297050	-406.697560	-415.940872	-404.885802	
log (Like)		-402.629727	-408.960474	-408.454977	2.467315	-412.097485	-406.520548	-415.757993	-404.678963	
log (Prior)		-0.203442	-0.163596	-0.147311	0.100964	-0.296183	-0.073908	-0.485685	-0.023113	
$M_\star$	[$M_\odot$]	0.980358	0.800314	0.788707	0.088192	0.701466	0.900776	0.600351	0.999712	$\mathcal{N}(0.8, 0.1)$
$\sigma_{JIT\ LOW}$	[m s^{-1}]	1.20	1.24	1.21	0.42	0.76	0.78	0.16	0.39	$\mathcal{U}$
$\sigma_{JIT\ HIGH}$	[m s^{-1}]	2.04	1.94	1.99	0.52	1.30	1.49	0.31	1.06	$\mathcal{U}$
γ_{HARPS}	[m s^{-1}]	39977.30	39977.24	39977.20	0.10	39977.12	39977.35	39977.00	39977.47	$\mathcal{U}$
RHK_{index} *lin*	[m s^{-1} $RHD_{index}{}^{-1}$]	3.902459	4.129760	4.057943	0.501237	3.567302	4.713965	2.972341	5.281426	$\mathcal{U}$
log (P)	[d]	1.148361	1.148375	1.148387	0.000043	1.148326	1.148424	1.148275	1.148474	$\mathcal{U}$
log (K)	[m s^{-1}]	0.61	0.60	0.60	0.02	0.58	0.61	0.56	0.63	$\mathcal{U}$
$\sqrt{e}.\cos\omega$		-0.118480	-0.123787	-0.183326	0.102911	-0.229128	0.007749	-0.308200	0.133668	$\mathcal{U}$
$\sqrt{e}.\sin\omega$		0.335597	0.239601	0.269015	0.095793	0.113091	0.322123	-0.059036	0.387245	$\mathcal{U}$
λ_0	[deg]	257.734884	257.274281	256.797681	2.077620	254.933378	259.655465	252.551371	262.119813	$\mathcal{U}$
log (P)	[d]	1.981979	1.982021	1.981746	0.000578	1.981402	1.982724	1.980805	1.983426	$\mathcal{U}$
log (K)	[m s^{-1}]	0.37	0.37	0.37	0.03	0.34	0.40	0.30	0.43	$\mathcal{U}$
$\sqrt{e}.\cos\omega$		-0.370075	-0.326983	-0.359983	0.111428	-0.420448	-0.181879	-0.492776	0.046683	$\mathcal{U}$
$\sqrt{e}.\sin\omega$		-0.080548	-0.087455	-0.136843	0.149558	-0.250395	0.099871	-0.366481	0.262974	$\mathcal{U}$
λ_0	[deg]	-160.261307	-158.719759	-159.674199	3.735633	-162.883613	-154.431466	-167.054572	-149.921315	$\mathcal{U}$

Table B.8. Parameters probed by the MCMC used to fit the RV measurements of HD134060. The maximum likelihood solution (Max(Like)), the median (Med), mode (Mod) and standard deviation (Std) of the posterior distribution for each parameter is shown, as well as the 68.3% (CI(15.85),CI(84.15)) and 95.45% (CI(2.275),CI(97.725)) confidence intervals. The prior for each parameter can be of type: $\mathcal{U}$: uniform, $\mathcal{N}$: normal.

Param.	Units	Max(Like)	Med	Mod	Std	CI(15.85)	CI(84.15)	CI(2.275)	CI(97.725)	Prior
					Likelihood					
log (Post)		-298.850697	-304.216566	-304.307005	2.241852	-307.134697	-302.087246	-310.611617	-300.536513	
log (Like)		-297.620659	-302.893646	-302.472853	2.232698	-305.807282	-300.789692	-309.374131	-299.237149	
log (Prior)		-1.230038	-1.253327	-1.227765	0.254368	-1.556962	-1.023282	-2.140093	-0.820972	
$M_\star$	[$M_\odot$]	1.099460	1.094932	1.086339	0.088166	0.993140	1.195814	0.898980	1.298334	$\mathcal{N}(1.095, 0.1)$
σ_{JIT}	[m s^{-1}]	1.58	1.65	1.63	0.22	1.43	1.35	1.31	1.04	$\mathcal{U}$
γ_{HARPS}	[m s^{-1}]	37987.94	37987.95	37987.91	0.13	37987.80	37988.10	37987.65	37988.25	$\mathcal{U}$
log (P)	[d]	0.514500	0.514500	0.514499	0.000011	0.514488	0.514512	0.514478	0.514526	$\mathcal{U}$
log (K)	[m s^{-1}]	0.67	0.66	0.66	0.02	0.64	0.68	0.62	0.70	$\mathcal{U}$
$\sqrt{e}.\cos\omega$		-0.125031	-0.096070	-0.087114	0.067809	-0.173750	-0.018918	-0.246029	0.063097	$\mathcal{U}$
$\sqrt{e}.\sin\omega$		-0.673348	-0.660554	-0.664313	0.027638	-0.690593	-0.628249	-0.720202	-0.591182	$\mathcal{U}$
λ_0	[deg]	-60.971221	-60.219046	-60.857964	2.817351	-63.378221	-57.046679	-66.686867	-53.740675	$\mathcal{U}$
log (P)	[d]	3.115614	3.111116	3.110321	0.013896	3.095987	3.126974	3.080422	3.146266	$\mathcal{U}$
log (K)	[m s^{-1}]	0.19	0.22	0.22	0.05	0.15	0.27	0.08	0.33	$\mathcal{U}$
$\sqrt{e}.\cos\omega$		0.018089	-0.131288	-0.033631	0.237542	-0.408103	0.151476	-0.601802	0.365222	$\mathcal{U}$
$\sqrt{e}.\sin\omega$		-0.193191	-0.102419	-0.157397	0.182951	-0.296909	0.130699	-0.452167	0.321316	$\mathcal{U}$
λ_0	[deg]	-57.886308	-59.605407	-62.436000	6.753625	-66.940199	-51.615752	-74.094300	-42.949848	$\mathcal{U}$

Table B.9. Parameters probed by the MCMC used to fit the RV measurements of HD136352. The maximum likelihood solution (Max(Like)), the median (Med), mode (Mod) and standard deviation (Std) of the posterior distribution for each parameter is shown, as well as the 68.3% (CI(15.85),CI(84.15)) and 95.45% (CI(2.275),CI(97.725)) confidence intervals. The prior for each parameter can be of type: $\mathcal{U}$: uniform, $\mathcal{N}$: normal.

Param.	Units	Max(Like)	Med	Mod	Std	CI(15.85)	CI(84.15)	CI(2.275)	CI(97.725)	Prior
					Likelihood					
log (Post)		-413.840756	-420.573939	-420.519231	2.525979	-423.752736	-418.071226	-427.592767	-416.139887	
log (Like)		-413.418243	-420.301368	-420.080839	2.517934	-423.494074	-417.796941	-427.287283	-415.883659	
log (Prior)		-0.422514	-0.225282	-0.181747	0.168419	-0.456156	-0.087916	-0.795628	-0.025262	
$M_\star$	[$M_\odot$]	0.836645	0.811051	0.810685	0.088144	0.710931	0.910337	0.609205	1.008754	$\mathcal{N}(0.81, 0.1)$
σ_{JIT}	[m s^{-1}]	1.43	1.41	1.41	0.30	1.02	1.08	0.76	0.81	$\mathcal{U}$
γ_{HARPS}	[m s^{-1}]	-68709.12	-68709.03	-68709.05	0.08	-68709.13	-68708.94	-68709.22	-68708.84	$\mathcal{U}$
log (P)	[d]	1.063786	1.063799	1.063829	0.000081	1.063703	1.063890	1.063608	1.063979	$\mathcal{U}$
log (K)	[m s^{-1}]	0.23	0.20	0.19	0.03	0.16	0.24	0.12	0.27	$\mathcal{U}$
$\sqrt{e}.\cos\omega$		-0.342695	-0.314967	-0.410810	0.145521	-0.437347	-0.116554	-0.524238	0.125811	$\mathcal{U}$
$\sqrt{e}.\sin\omega$		-0.090658	0.033773	0.091648	0.156779	-0.152919	0.214589	-0.306061	0.352353	$\mathcal{U}$
λ_0	[deg]	277.740369	277.024300	275.232882	4.443846	272.023532	282.083700	266.558482	287.198688	$\mathcal{U}$
log (P)	[d]	1.440604	1.440627	1.440596	0.000121	1.440492	1.440768	1.440359	1.440909	$\mathcal{U}$
log (K)	[m s^{-1}]	0.43	0.42	0.42	0.02	0.40	0.45	0.37	0.47	$\mathcal{U}$
$\sqrt{e}.\cos\omega$		-0.070645	-0.042094	-0.084481	0.126899	-0.182267	0.113998	-0.296099	0.237968	$\mathcal{U}$
$\sqrt{e}.\sin\omega$		-0.212716	-0.113587	-0.193076	0.134373	-0.259032	0.060329	-0.348573	0.197605	$\mathcal{U}$
λ_0	[deg]	19.705439	19.919436	19.941697	2.590743	16.987116	22.886544	14.008324	25.935025	$\mathcal{U}$
log (P)	[d]	2.030837	2.031806	2.031583	0.000968	2.030727	2.032933	2.029701	2.034155	$\mathcal{U}$
log (K)	[m s^{-1}]	0.12	0.13	0.12	0.04	0.08	0.17	0.03	0.22	$\mathcal{U}$
$\sqrt{e}.\cos\omega$		-0.489331	-0.199704	-0.273372	0.203550	-0.406230	0.080327	-0.542331	0.280257	$\mathcal{U}$
$\sqrt{e}.\sin\omega$		0.029048	0.037665	0.048956	0.162724	-0.157033	0.224967	-0.309643	0.370264	$\mathcal{U}$
λ_0	[deg]	185.975741	188.581732	187.252622	5.246122	182.652564	194.619420	176.751015	200.688274	$\mathcal{U}$